Unlocking Molecular Secrets in a Monomer-Assembly-Promoted Zn-Metalated Catalytic Porous Organic Polymer for Light-Responsive CO_2 Insertion

Chitra Sarkar,° Ratul Paul,° Duy Quang Dao, Shaojun Xu, Rupak Chatterjee, Subhash Chandra Shit, Asim Bhaumik, and John Mondal*

ABSTRACT: Anthropogenic carbon dioxide (CO_2) emission is soaring day by day due to fossil fuel combustion to fulfill the daily energy requirements of our society. The CO_2 concentration should be stabilized to evade the deadly consequences of it, as climate change is one of the major consequences of greenhouse gas emission. Chemical fixation of CO_2 to other value-added chemicals requires high energy due to its stability at the highest oxidation state, creating a tremendous challenge to the scientific community to fix CO_2 and prevent global warming caused by it. In this work, we have introduced a novel monomer-assembly-directed strategy to design va isible-light-responsive conjugated Zn-metalated porous organic polymer (Zn@MA-POP) with a dynamic covalent acyl hydrazone linkage, via a one-pot condensation between the self-assembled monomer 1,3,5-benzenetricarbohydrazide (TPH) and a Zn complex (Zn@COM). We have successfully explored as-synthesized Zn@MA-POP as a potential photocatalyst in visible-light-driven CO_2 photofixation with styrene epoxide (SE) to styrene carbonate (SC). Nearly 90% desired product (SC) selectivity has been achieved with our Zn@MA-POP, which is significantly better than that for the conventional Zn@TiO_2 (~29%) and Zn@gC_3N_4 (~26%) photocatalytic systems. The excellent light-harvesting nature with longer lifetime minimizes the radiative recombination rate of photoexcited electrons as a result of extended π-conjugation in Zn@MA-POP and increased CO_2 uptake, eventually boosting the photocatalytic activity. Local structural results from a first-shell EXAFS analysis reveals the existence of a Zn(N_2O_4) core structure in Zn@MA-POP, which plays a pivotal role in activating the epoxide ring as well as capturing the CO_2 molecules. An in-depth study of the POP–CO_2 interaction via a density functional theory (DFT) analysis reveals two feasible interactions, Zn@MA-POP-CO_2-A and Zn@MA-POP-CO_2-B, of which the latter has a lower relative energy of 0.90 kcal/mol in comparison to the former. A density of states (DOS) calculation demonstrates the lowering of the LUMO energy (EL) of Zn@MA-POP by 0.35 and 0.42 eV, respectively, for the two feasible interactions, in comparison to Zn@COM. Moreover, the potential energy profile also unveils the spontaneous and exergonic photoconversion pathways for the SE to SC conversion. Our contribution is expected to spur further interest in the precise design of visible-light-active conjugated porous organic polymers for CO_2 photofixation to value-added chemicals.

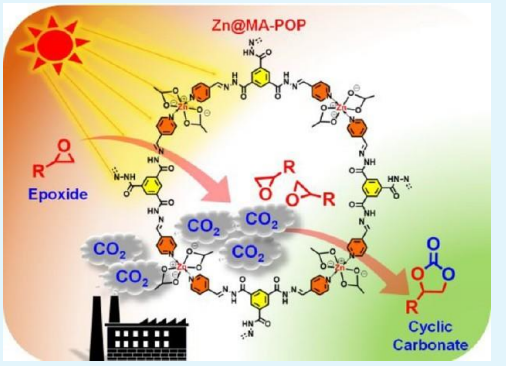

KEYWORDS: *CO_2 cycloaddition, metalated porous organic polymer, CO_2 photofixation, photopolymer, monomer assembly*

INTRODUCTION

Anthropogenic CO_2 emission due to the fossil fuel combustion during continuous industrial development gives rise to greenhouse gases in the Earth's atmosphere. For the first time in human history, the atmospheric level of CO_2 recently escalated abruptly more than 415 ppm in our planet.[1] This rapid growth of atmospheric CO_2 not only disrupts livelihoods through the havoc of climate change but also damages the food supply chain and causes the death of a huge number of animals during forest fired every year. Hence, the development of sustainable energy sources to curb industrial/social needs and lowering the environmental pollution have been a challenge to the scientific community in these recent years. Currently two methods are available for CO_2 mitigation: i.e., CO_2 capture from the atmosphere accompanied by either storage or transformation to a feedstock of fuel and value-added chemicals.[2−5] Of all the utilization processes, CO_2 insertion into an epoxide to form a nontoxic/nonflammable cyclic carbonate is the most attractive due to its economic viability

Scheme 1. Schematic Illustration of the Synthesis of a Zn-Metalated Porous Organic Polymer (Zn@MA-POP) and Its Photoresponsive CO_2 Fixation Activity

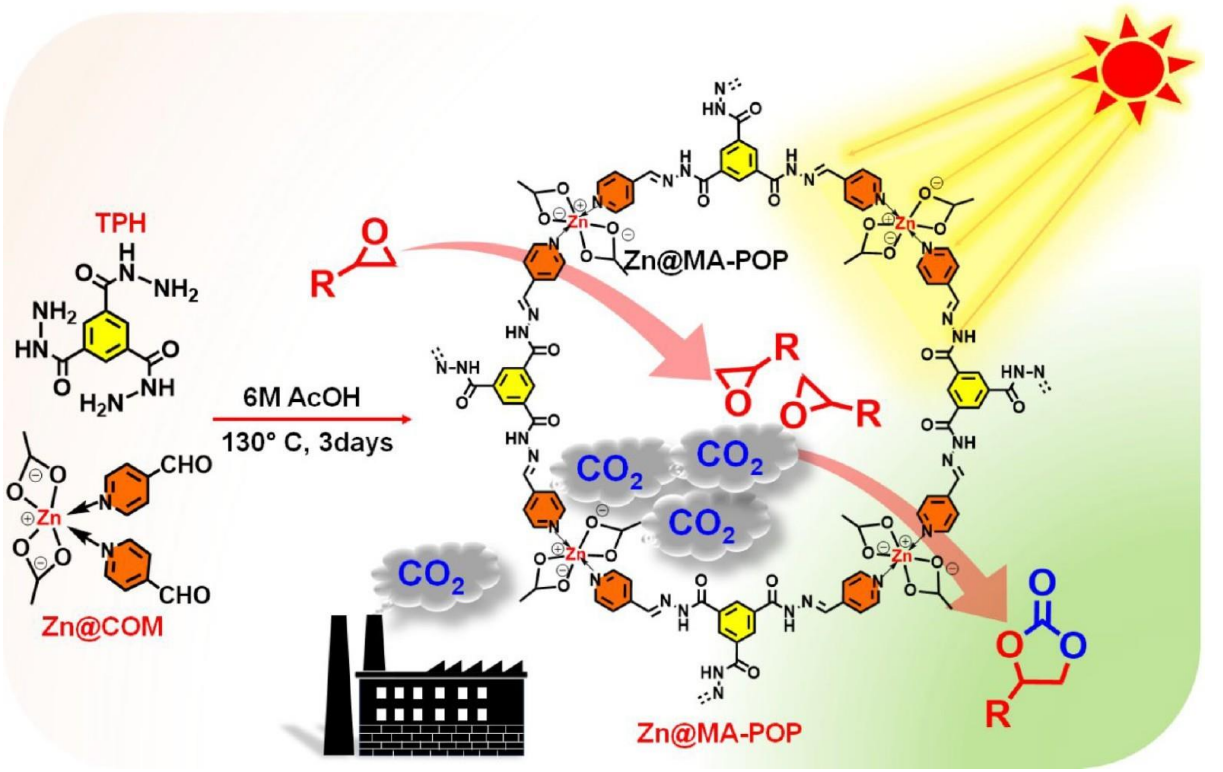

with 100% atom economy. There are various other advantages of utilization of CO_2 to form a cyclic carbonate formation, as it can be used as a replacement for toxic phosgene gas and also deployed as an essential monomer for polycarbonates and polyurethanes.[6−8] Up to now various effective catalysts based on stable materials such as zeolite, silica, hydrotalcite, metal−organic frameworks, and graphene oxide have been developed for the insertion of CO_2 into oxirane utilizing harsh reaction conditions.[9−13] Hence, it is extremely important to enable the activation of a catalyst under mild reaction conditions.

Porous organic polymers (POPs) possesses chemical tunability due to a wide range of building blocks accompanied by high surface area as well as high chemical and thermal stability, low skeletal density, and adjustable chemical functionalities, which have attracted the attention of recent researchers to exploit the pressing needs of developing multifunctional materials, utilized in various fields ranging from gas adsorption and separation to catalysis.[14−20] Furthermore, POPs will be ideal candidates to illustrate their CO_2 adsorption capacity as well as visible-light-driven CO_2 fixation[21] ability due to the presence of abundant heteroatoms for strong CO_2 affinity and π-electron delocalization in the extended conjugated framework nanoarchitecture that can easily create photogenerated electrons. POPs with extended π-conjugations also exhibit a wider visible-light absorption range and a more tunable position of the valence band (VB) and conduction band (CB) in comparison with inorganic semiconductor materials, which provides a unique opportunity to bridge the gap between sustainability and efficiency in the field of heterogeneous photocatalysis. For the photocatalytic CO_2 insertion in oxirane, epoxide ring opening appeared to be the rate-determining step.[22] Various types of Lewis acidic sites (Zn, Al, Co) accelerate the adsorption of epoxide, which further enabled the nucleophilic attack of a cocatalyst such as 4-dimethylaminopyridine (DMAP) or tetrabutylammonium bromide (TBAB).[17] However, linear CO_2 is a stable molecule with a high enthalpy of C=O (+805 kJ mol^{-1}). Thus, the activation of CO_2 during photocatalysis by introducing a metal site on the POP framework appears to be a productive way to create a stable photocatalyst. To date, very few catalysts have been designed and reported for the visible-light-triggered cycloaddition of CO_2 and oxirane.[23,24] However, the developed photocatalysts are still experiencing profound shortcomings in performance because of low CO_2 adsorption capacity, poor CO_2 activation ability, and catalyst photocorrosion tendency.

In this context, a thriving monomer-assembly-promoted approach has been presented to rationally construct a new class of metalated POP having a dynamic covalent acyl hydrazone linkage showing visible-light responsiveness. In this strategy, the emergence of Zn@MA-POP was promoted by the condensation reaction of self-assembled microfiber bundles of 1,3,5-benzenetricarbohydrazide (TPH) and a Zn complex (Zn@COM). The extended π-conjugation throughout the polymeric network exerts an appreciable effect on the high electron drift mobility, leading to a broadened visible-light-responsive range, reduction of the possibility of charge recombination, and a higher lifetime of the photo excitons. As envisaged, Zn@MA-POP exhibited superior activity for visible-light-driven CO_2 photofixation in comparison with the various conventional catalysts. To the best of our knowledge, this is the first report on a monomer-self-assembly-directed synthesis and utilization of a visible-light-responsive Zn-metalated POP for CO_2 insertion to cyclic carbonates. Furthermore, the structure−activity relationship was estab-

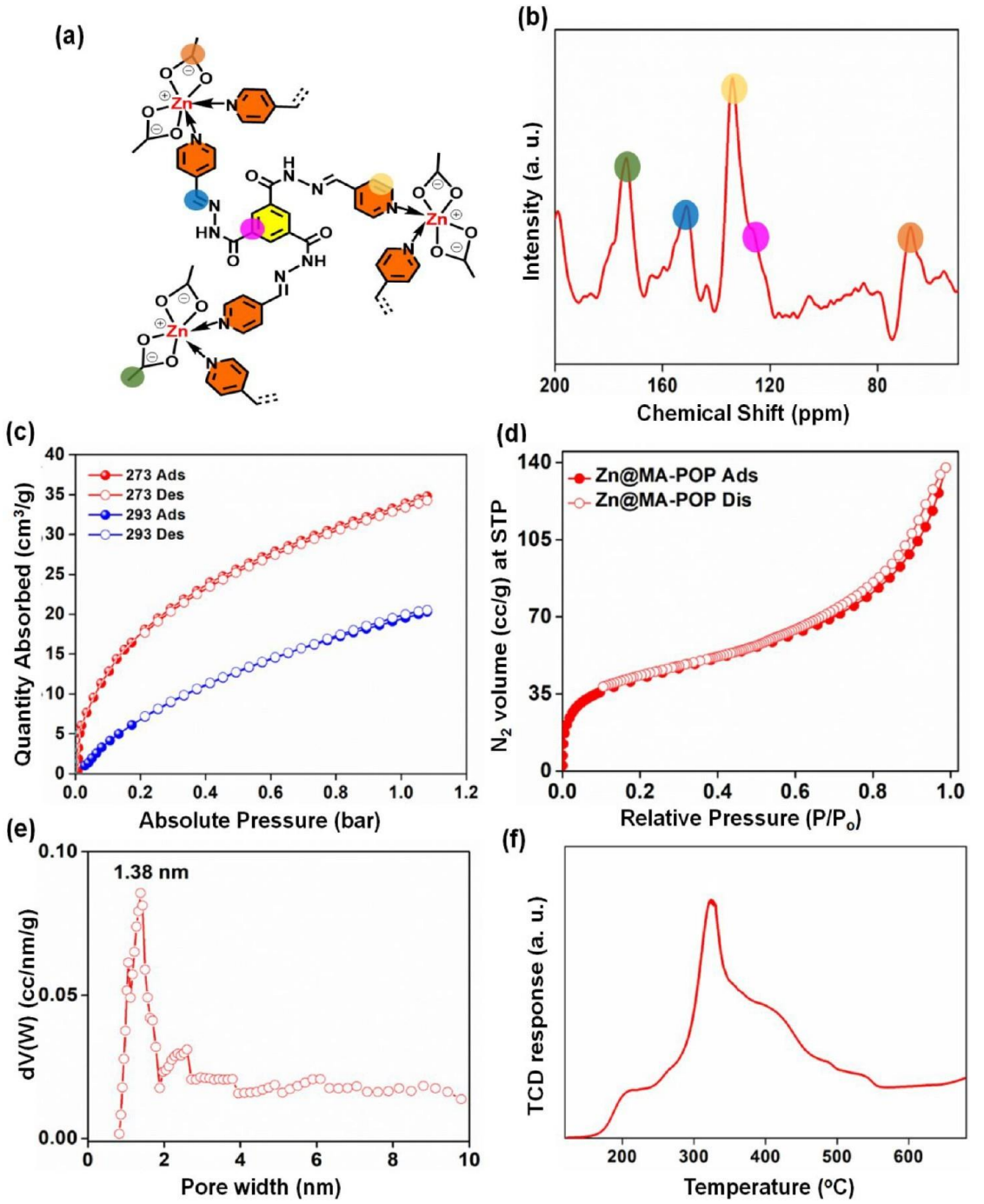

Figure 1. Structural integrity unit (a), ^{13}C CP solid-state MAS NMR spectrum (b), CO_2 adsorption/desorption isotherms analysis at 273 and 298 K (c), N_2-adsorption/desorption isotherm analysis at 77 K (d), the corresponding pore-size distribution as measured by the NLDFT method (e), and NH_3-TPD analysis (f) of Zn@MA-POP.

lished by XAFS analysis and a DFT computational study to get a detailed insight into the impressive photocatalytic activity of our Zn@MA-POP. Activation of CO_2 on the ZnN_2O_4 catalytic core of Zn@MA-POP was initiated through complexation of the CO_2 molecule into two different positions, O1/O3 (Zn@MA-POP-CO_2-A) or O2/O3 (Zn@MA-POP-CO_2-B); however, the former exhibited higher relative energy (0.90 kcal/mol) in comparison to the latter, confirming that the interaction proceeds via the O2/O3 position. Moreover, the whole reaction process including the formation of several intermediates utilizing our Zn@MA-POP for SE to SC conversion is spontaneous and exergonic in nature and the polymeric network of Zn@MA-POP exhibits superior light-harvesting ability in CO_2 photofixation in comparison to its monomeric counterpart (Zn@COM).

RESULTS AND DISCUSSION

Catalyst Synthesis and Characterization. As illustrated in Scheme 1, we have initiated a novel monomer-assembly-directed strategy where the consequential hydrogen-bonding and π–π interactions in 1,3,5-benzenetricarbohydrazide (TPH) monomer eventually encourage a self-assembly

behavior. The concomitant reaction between trimethyl-1,3,5-benzenetricarboxylate and hydrazine hydrate in methanol leads to the evolution of a microtubular structure of TPH.[22] Zn@COM was synthesized *via* a complexation reaction between Zn(acetate)$_2$ and 4-pyridinecarboxaldehyde. Furthermore, the one-pot polycondensation reaction between the Zn complex (Zn@COM) and TPH facilitates the formation of the conjugated Zn@MA-POP *via* the dynamic covalent acyl hydrazone linkage. Interestingly, addition of Zn@COM to a solution containing TPH effectuates extended organic polymeric network units with porosity accompanied by the three carbohydrazide units as constructed through a Schiff base condensation reaction with the help of an acetic acid catalyst. In the first step, nucleophilic addition of the aromatic hydrazide and the pyridinecarboxaldehyde-based zinc complex accelerates the formation of hemiaminal units. Then, dehydration of the hemiaminal intermediate promotes the formation of a porous framework through the imine bonds. The detailed synthesis procedure of TPH, Zn@COM monomer, and Zn@MA-POP are provided in Figures S1–S3 in the Supporting Information. The structural integrity unit of the respective Zn@MA-POP is depicted in Figure 1a.

Nanostructure Elucidation. Wide-angle powder X-ray diffraction (PXRD) is a technique that reveals diffraction planes present in a sample. A PXRD analysis of the fiber monomer showed sharp peaks at $2\vartheta = 9.8$, 19.47, and 22.9°, respectively, due to the typical lamellar phase with very highly crystalline nature (Figure S4 in the Supporting Information).[22] For the Zn@MA-POP framework, the appearance of a broad peak in the low-2ϑ region demonstrates the amorphous nature of the POP skeleton (Figure S5 in the Supporting Information). The two distinct broad peaks appearing at 26.4 and 41° could be assigned to the (002) and (101) carbon planes, respectively, corresponding to the π-stacking interaction of aromatic building units within a small domain due to the random polymerization method between two monomers.[22] The absence of peaks corresponding to ZnO crystalline planes and the presence of broad peaks around $2\vartheta = 20°$ in the wide-angle PXRD analysis of Zn@MA-POP clearly indicate the amorphous nature of our POP, thereby diminishing the formation of the ZnO phase (Figure S5 in the Supporting Information).[25] A ^{13}C CP solid-state MAS NMR spectral analysis (Figure 1b) has been conducted to understand the molecular connectivity along with the chemical environment of each discrete carbon atom present in the molecular assembly of Zn@MA-POP. The existence of a distinct resonance signal at δ 173.6 ppm indicates the signature of the C=O bond of the tricarbohydrazide unit. Furthermore, the successful polymerization between 1,3,5-benzenetricarbohydrazide (TPH) and the zinc pyridine complex (Zn@COM) was confirmed through the presence of the signature band of the hydrazone linkage at δ 151 ppm. A broad peak in the region of 120–138 ppm confirms the presence of aromatic carbon atoms of pyridine and the TPH unit.[24] In addition, the existence of the characteristic signal of an aliphatic methyl carbon of Zn@COM was noted at δ 21.2 ppm, confirming the efficient polymerization between two monomers through a one-step polycondensation method. To monitor the formation of the covalent acyl hydrazone linkage in our as-synthesized Zn@MA-POP, we have used the Fourier-transform infrared (FT-IR) spectroscopy technique (Figure S6 in the Supporting Information). The appearance of distinct characteristic peaks at 1263, 1620, and 1710 cm^{-1}, respectively, confirms the existence of −N−N, −C=N−, and −C=O in our as- synthesized hydrazone-linked Zn@MA-POP material, clearly indicating the successful incorporation of monomeric units through the one-step polycondensation reaction.[26−28] Additionally, the stretching vibration peak appearing at 3240 cm^{-1} corresponds to the −NH bond of a secondary amine adjacent to a acyl group. As CO_2 adsorption on the catalyst surface is the pivotal parameter for CO_2 conversion into value-added chemicals and fuels, we have investigated the CO_2 uptake capacity of our as-synthesized Zn@MA-POP at two different temperatures (273 and 298 K). In order to maximize the CO_2 uptake capacity over the porous adsorbents, an improvement in the surface CO_2-philicity of the porous network is immensely significant. The functionalization of the porous framework could be initiated by incorporating a heteroatom or an other functional group to generate an electrostatic field on the surface and porous channels of POP, which is responsible for the significant interaction between CO_2 and the host POP material.[29] Actually, the appearance of atoms and functional groups on the materials promotes a dipole−quadrupole interaction, which improves the CO_2-philicity of the porous surface. Herein, our as-synthesized acyl hydrazone linked Zn@MA-POP exhibited an CO_2 uptakes of 1.53 and 0.89 mmol/g at 273 and 298 K, respectively, up to 1 bar pressure, as shown in Figure 1c. The enhancement in diffusion of CO_2 from the gas-bulk flow to the adsorbent surface with increasing temperature leads to a drop in CO_2 adsorption capacity. We have also observed the sharp increase of CO_2 adsorption in the lower pressure region, which is due to the appearance of strong polarizing sites (heteroatoms) on the Zn@MA-POP surface. In order to illustrate this phenomenon, the isosteric heat of adsorption (Q_{st}) has been calculated with the help of a virial method, provided in Figure S7b in the Supporting Information. The CO_2 adsorption with the virial equation fit at two different temperatures is shown in Figure S7a in the Supporting Information. The calculated Q_{st} value appeared to be 55 kJ/mol, demonstrating the good CO_2 affinity of our Zn@MA-POP, which definitely has an influence on the CO_2 utilization reaction. An N_2 adsorption/desorption isotherm analysis at 77 K for Zn@MA-POP has been performed to evaluate the permanent inherent porosity developed during extended polymerization. Zn@MA-POP exhibited a typical type IV isotherm profile with sharp gas uptake at low pressures (P/P_0 = 0.0–0.04), followed by an exponential increase of gas uptake in the higher pressure region (P/P_0 = 0.6–0.8) with no hysteresis loop, indicating the existence of micropores in the nanoscale dimension (Figure 1d).[30,31] The obtained Brunauer–Emmett–Teller (BET) surface area of Zn@MA-POP appeared to be 156 m^2/g with a corresponding pore volume of about 0.1954 cm^3/g. Furthermore, nonlocal density functional theory (NLDFT) has been employed to calculate the pore size distribution (PSD) pattern (Figure 1e). The narrow pore size distribution, with predominantly micropores having a width of 1.38 nm, clearly demonstrates the microporous nature of our Zn@MA-POP. NH_3-temperature programmed desorption (NH_3-TPD) for the heterogeneous catalytic system has been used to evaluate the surface acidity by measuring the acidic sites on the surface. NH_3-TPD profiles were primarily divided into three categories based on temperature, denoted as weak (150–300 °C), medium (300–500 °C), and strong (500–650 °C), respectively. According to Pearson's HSAB classification, Zn(II) complexes possess a borderline Lewis acidic character and as a consequence of this unique conventional theory, the

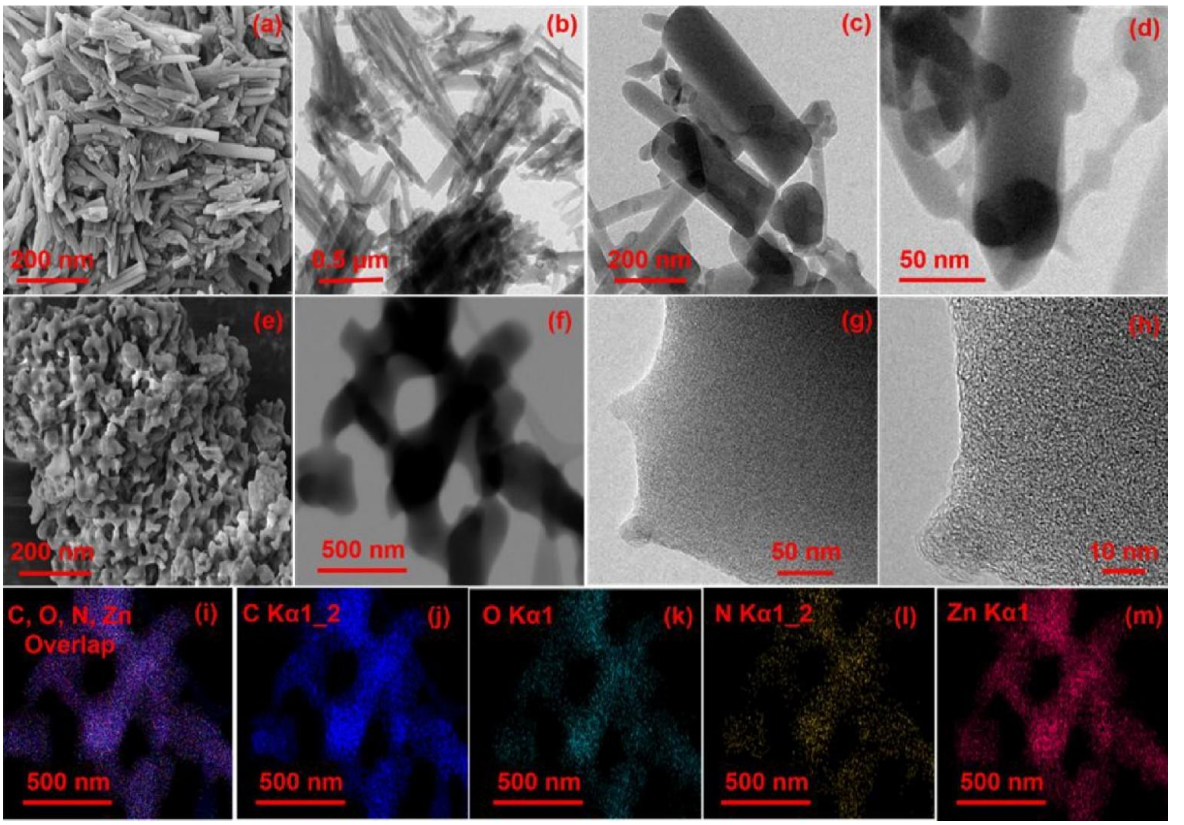

Figure 2. FE-SEM images of TPH (a) and Zn@MA-POP (e). TEM images of TPH (b–d) and Zn@MA-POP (f–h), along with the corresponding elemental maps of C (blue), O (green), N (yellow), and Zn (red) images (i–m).

NH_3-TPD profile of Zn@MA-POP exhibited a broad peak at 300–440 °C (Figure 1f).The calculated total acid strength of Zn@MA-POP appeared to be 0.801 mmol/g. This acidic zinc site is thought to activate the epoxide ring during photocatalytic CO_2 insertion into the styrene epoxide (SE).[32,33] A thermogravimetric analysis (TGA) (Figure S8 in the Supporting Information) revealed a high thermal stability up to 200 °C, followed by a sharp weight loss of 60 wt % with an increase in temperature until 400 °C due to the breakdown of the polymeric framework. This demonstrates the high thermal stability of Zn@MA-POP until 200–220 °C. Furthermore, an inductively coupled plasma optical emission spectrometry (ICP-OES) analysis illustrates Zn content in the polymeric framework is 10.49 wt %, which is comparatively lower than the theoretical value of 11.4 wt %.

Morphology Analysis. Field-emission scanning electron microscopy (FE-SEM) images of the respective TPH and Zn@MA-POP were obtained to reveal the very small topographic details of the surface. The assembled structure of microtubular bundles with an average length of 200–400 nm and width of 45–80 nm corresponding to the TPH monomer can be clearly seen in Figure 2a. However, an aggregated clustered island was noted in case of the TPH monomer, as shown in Figure S9a,b in the Supporting Information. However on a closer inspection of the FE-SEM image, a random arrangement of microtubular tubular bundles in different dimensions was seen, as shown in Figure S9c in the Supporting Information. On the other hand, the FE-SEM image of Zn@MA-POP clearly illustrates the incorporation of Zn@COM with TPH bundles by forming a sponge type of morphology through stacking of each layer with another (Figure 2e). An energy dispersive X-ray (EDX) analysis in a selected area of the FE-SEM image of Zn@MA-POP demonstrates the concomitant appearance of C, Zn, O, and N elements, respectively (Figure S10 in the Supporting Information).

A transmission electron microscopy (TEM) analysis was performed for a further inspection of the surface topography. Densely packed tubular bundles with a hollow interior prevailed in the TEM image of the TPH unit (Figure 2b). In some cases, the greater length of highly flexible TPH bundles leads to bending (Figure 2c,d), clearly illustrating the flexibility of microtubular bundles with diameters in the 10–40 nm range by a line-to-line fusion amidst the tubes. Interestingly, the incorporation of Zn@COM with the hollow/highly flexible TPH unit through polycondensation gives rise to the formation of a sponge type of structure through bending (Figure 2f). Additionally, the metal complex is fully encapsulated by the hollow tubular skeleton of the TPH framework, denoted by the darker region in the TEM image of Zn@MA-POP. The presence of well-defined micropores throughout the polymeric framework can be seen in high-resolution TEM (HR-TEM) images of Zn@MA-POP (Figure 2g,h). According to Figure 2h, the micropores are in the range of 1–2 nm, which correlates to the PSD analysis previously provided (Figure 1e). The absence of crystalline fringes demonstrates the amorphous nature of our metalated POP, coinciding with PXRD data. An elemental mapping analysis has been performed to obtain the abundance of each individual element on the POP surface. Figure 2i indicates the appearance of all elements, where each element was specified with an individual color such as C (blue), O (green), N (yellow), and Zn (red) images. However, the nearly

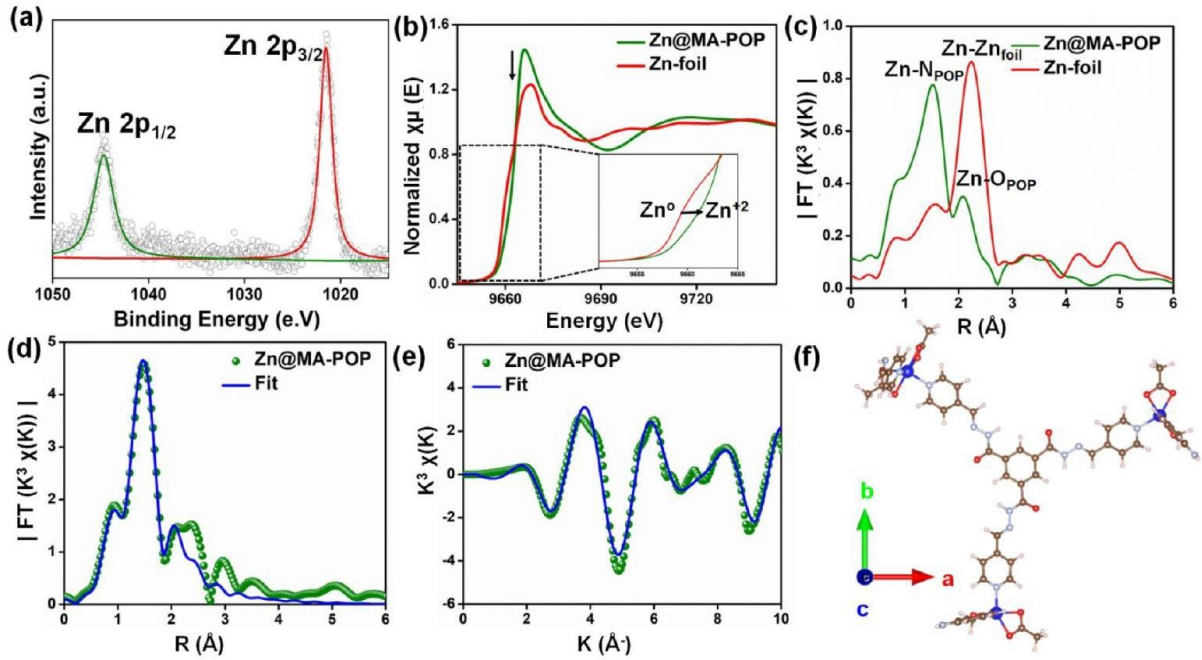

Figure 3. Core level Zn 2p XP spectrum (a), Zn K-edge X-ray absorption near edge structure (XANES) spectra (b), Fourier transform magnitudes of the Zn K-edge FT-EXAFS, showing the local atomic distributions around Zn in Zn@MA-POP and Zn-foil (c). The corresponding Zn−N/O first-shell EXAFS fitting curves at *R* space (d) and *k* space (e) and optimized geometry of Zn@MA-POP (f): Zn (blue), O (red), and N (sky blue).

homogeneous dispersion of all elements on the porous network was noted, as shown in Figure 2j−m, indicating the successful polymerization between monomeric counterparts.

XPS Study and EXAFS Analysis of Zn@MA-POP. The chemical composition of Zn@MA-POP was investigated using the X-ray photoelectron spectroscopy (XPS) technique. The XPS survey spectrum in the full scan range (Figure S11 in the Supporting Information) confirms the presence of Zn, C, N, and O elements and matches well with the corresponding EDX spectrum (Figure S10 in the Supporting Information). The Zn 2p core level XPS spectrum (Figure 3a) exhibits two distinct binding energy doublets located at ∼1044.8 eV (Zn $2p_{1/2}$) and ∼1021.6 eV (Zn $2p_{3/2}$), validating the existence of tetrahedral Zn^{2+} ions in Zn@MA-POP.[34] In the C 1s deconvoluted XP spectrum (Figure S12a in the Supporting Information), we observe two characteristic binding peaks at ∼284.4 and ∼286.27 eV, which could be assigned to C═C bonds, the C−N bonds of secondary amine moieties and C−O bonds, respectively.[35,36] The high-resolution N 1s XPS peaks (Figure S12b in the Supporting Information) appearing at ∼398.09, ∼398.91, and ∼400.1 eV, could be ascribed to −NH of the TPH unit, a Schiff base bond (−C═N) and pyridine N that is attached to Zn metal of the polymer unit, respectively.[37−39] The deconvoluted O 1s XPS spectrum (Figure S12c in the Supporting Information) demonstrates two distinct binding energy peaks at ∼532.7 and ∼530.9 eV, respectively, corresponding to the O atoms in the [C O−H] group and acetate group attached to Zn metal, respectively. Our observation is in accordance with a previous report by Li et al.[35,40]

To gain further insight into the electronic structure and the coordination environment of Zn in our as-synthesized Zn@MA-POP, we have conducted synchrotron-based extended X-ray absorption fine structure (EXAFS) and X-ray absorption near-edge structure (XANES) analyses. For the purposes of comparison, a series of experiments have been performed with respect to the standard Zn foil. A noticeable absorption edge shift at a higher energy level for Zn@MA-POP (Figure 3b) in comparison with the Zn foil has been observed from Zn K-edge X-ray absorption near-edge structure (XANES) spectra, which unambiguously indicates the higher oxidation state of Zn(II) in our Zn@MA-POP in comparison to Zn foil (Zn^0).[41] Moreover, we have also noticed that the white line intensity of our as-synthesized Zn@MA-POP increased in comparison to commercial Zn foil due to the decrease in electron density over Zn as result of electronic tuning between the active Zn site and the conjugated porous polymer support.[42] In the k^3-weighted Fourier transform (FT) of EXAFS spectra the major peak predominately arises at 2.07 Å, corresponding to the Zn−N bond (Figure 3c). Two types of Zn−O bonds appeared at 1.94 and 2.61 Å, respectively, which may be ascribed to the effective coordination of acetate units together. According to Tournilhac et al., the anhydrous zinc acetate complex has four Zn−O bonds. On the other hand, the hydrous zinc acetate complex has six Zn−O bonds, with two additional H_2O molecules occupying axial positions.[43] In our Zn@MA-POP, two N atoms from pyridine moieties occupy axial positions, while four O atoms from two acetate groups occupy four equatorial locations, resulting in a hexacoordinated ZnN_2O_4 core. The best-fitted EXAFS data of Zn@MA-POP (Figure 3d,e) at the respective *R* and *k* spaces illustrate the appearance of the ZnN_2O_4 core due to the coordination of the Zn^{2+} ion with two acetates and two pyridinic N moieties, the prevalent active species in the Zn@MA-POP framework. All of the corresponding coordination numbers (*N*) and the corresponding bond lengths (*R* (Å)) are provided in Table 1. The optimized core-level geometry of Zn@MA-POP demonstrates (Figure 3f) the existence of ZnN_2O_4 core, as supported by the EXAFS analysis.

Photophysical Properties of Zn@MA-POP. The photophysical properties of monomers and Zn@MA-POP were demonstrated by UV−vis diffuse reflectance spectroscopy

Table 1. Local Structural Results from the First-Shell EXAFS Analysis of Zn@MA-POP

first shell	coord. no. (N)	Bond length R (Å)
Zn-N5.1	2	2.071
Zn-O5.1	2	1.94
Zn-O4.1	2	2.61

(UV-vis-DRS) and steady-state photoluminescence (PL) analyses.Broad spectra in the medium-UV region (200−300 nm) were detected for the TPH unit and Zn@COM with absorption bands at 250 and 262 nm, respectively. However, after the polymer formation (Zn@MA-POP) the absorption band red-shifted to the visible region, indicating the good light-harvesting property of the conjugated polymer (Figure 4a).[44] However, the shoulder peak emerging at 694 nm certainly demonstrates the delocalized intramolecular charge transfer (ICT) through the π−π conjugation inside the highly conjugated porous polymer. The band gap of Zn@MA-POP has been calculated from a Tauc plot (Figure S13 in the Supporting Information) with the help of the Kubelka−Munk equation. The narrowest band gap of about 2.5 eV was found for Zn@MA-POP.[32] The steady-state PL spectra (Figure 4b) of TPH, Zn@COM, and Zn@MA-POP have been evaluated by exciting the materials at a wavelength of 350 nm, from which we obtained broad emission peaks at 500, 520, and 550 nm, respectively. After polymerization between TPH and Zn@COM the emission band red-shifted to 550 nm, attributed to a metal to ligand charge transfer (MLCT) transition for Zn@MA-POP.[45] The emission band shift is further reflected by the smallest band gap (E_g = 2.5 eV) for Zn@MA-POP in comparison to the other counterparts.[46] In addition, we have conducted a time-correlated single photon counting (TCSPC) analysis of Zn@MA-POP with 550 nm excitation (Figure4c) to calculate the excited-state PL decay. The obtained average lifetime (τ_{avg}) appeared to be 0.86 ns (Table S1 in the Supporting Information). Herein, the considerably longer lifetime clearly demonstrates the lower susceptibility of radiative recombination between photoexcited electrons as a consequence of extended π-conjugation in Zn@MA-POP.[47] To estimate the band edge locations of Zn@MA-POP, a Mott−Schottky analysis was performed (Figure 4d), which showed a positive slope of $1/C^2$ vs applied potential, characteristic of an n-type semiconductor.[48] The flat band potential of Zn@MA-POP calculated from the x intercept is −1.05 V.[49] For n-type semiconductors, the conduction band edge potential is defined as a drop in the flat band potential by 0.10 V, and hence the calculated CB/LUMO potential is −0.95 V. Further, the VB/HOMO position was found to be 1.55 V using the equation $E_{VB} - E_{CB} = E_g$.[50] The HOMO and LUMO distributions from a DFT analysis of the Zn@MA-POP unit (Figure 4e) along with the band alignment show that the HOMO is mainly localized on the TPH moiety, whereas the LUMO is delocalized across the Zn-core unit, which basically acts as an electron acceptor. This allows for the dissociation of photoexcitons across the conjugated photo-polymer. In addition, the electrostatic potential (ESP) map calculation (Figure 4f) shows that the most negatively charged zones shown in red are found at the Zn core, whereas the TPH unit displays the most positive charges as shown in blue. Similarly, the optimized geometries, HOMO−LUMO distributions, and the ESP maps for the TPH and Zn@COM are provided in Figures S14 and S15 in the Supporting Information. From a previous report by Alzamly et al. it was established that at least 0.73 eV is needed to activate the linear CO_2 molecule to $CO_2^{\bullet-}$.[51] Our as-developed Zn@MA-POP has enough potential to activate CO_2, which can then further

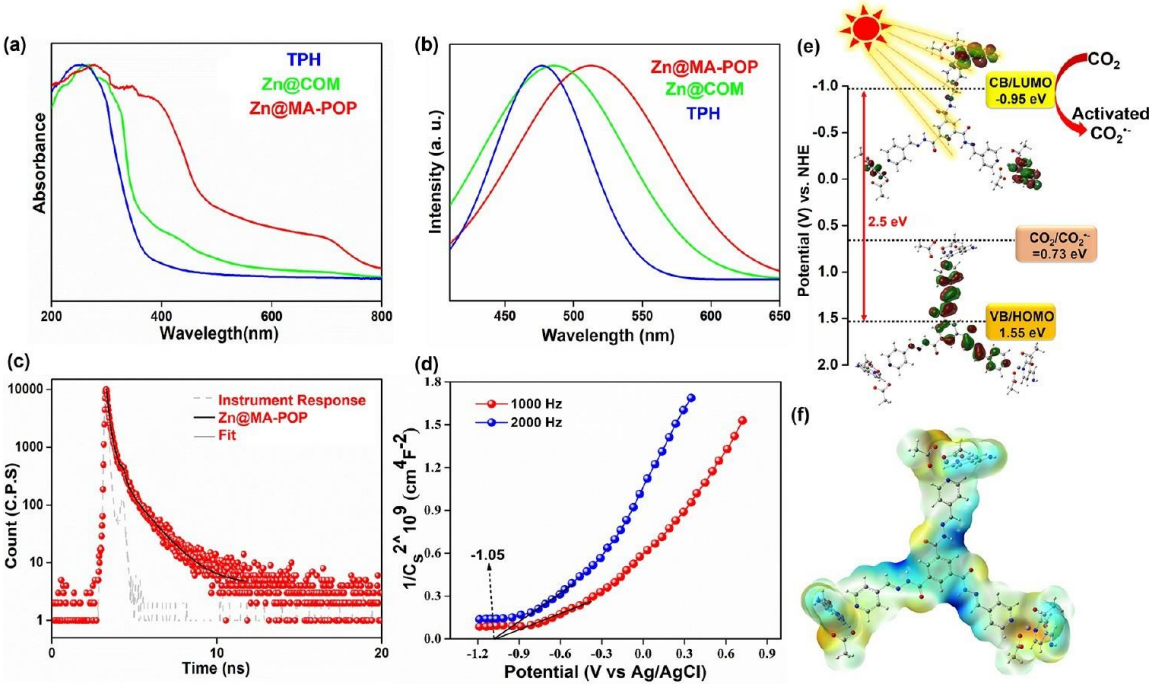

Figure 4. UV-vis-DRS absorption spectra (a), steady-state PL spectra (b), TCSPC analysis (c), Mott−Schottky plot (d), band alignment along with highest occupied molecular orbital (HOMO) and lowest unoccupied molecular orbital (LUMO) distributions (e), and electrostatic potential (ESP) mapping (f) of the Zn@MA-POP unit.

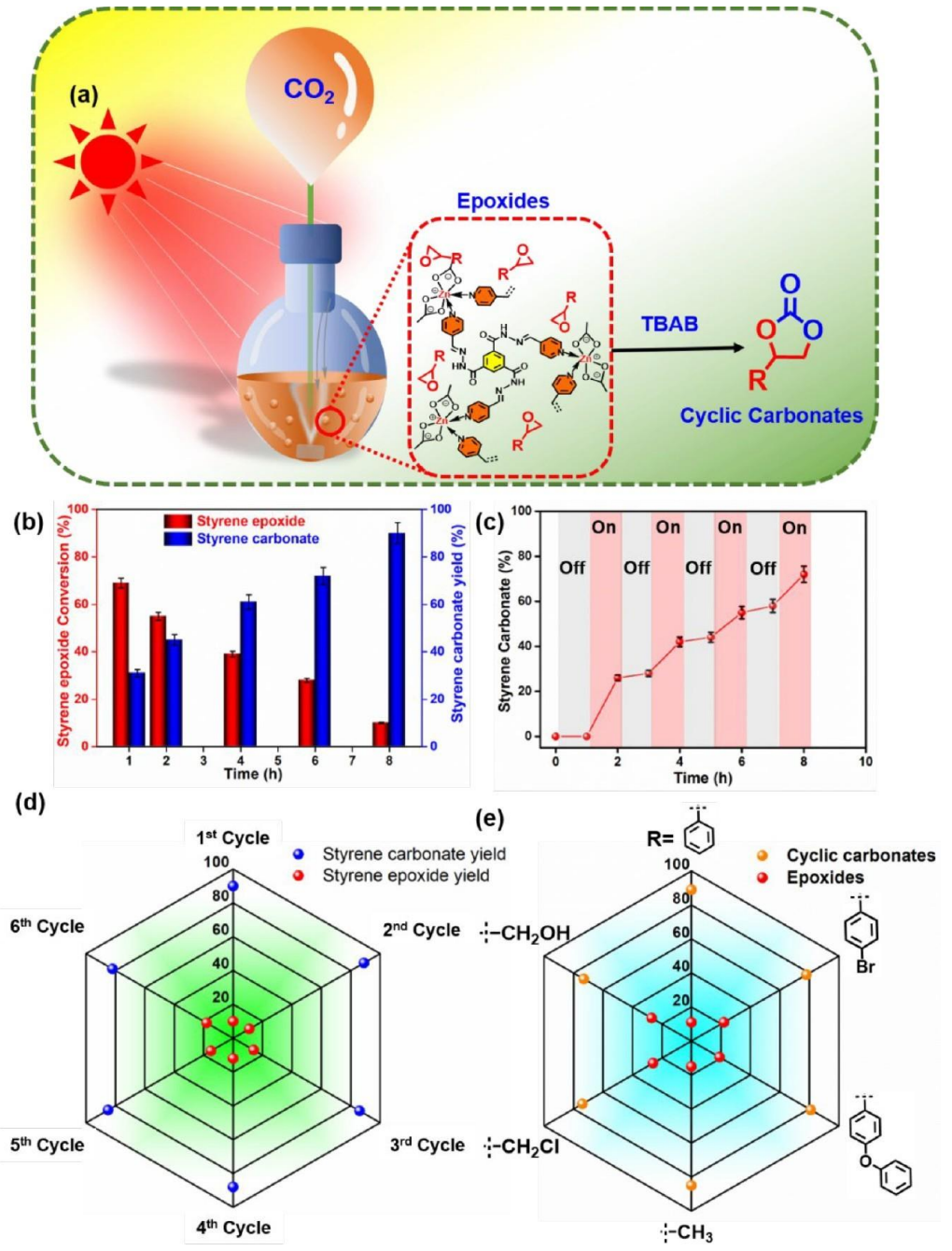

Figure 5. Schematic illustration of epoxide to cyclic carbonate formation *via* CO_2 insertion (a), conversion vs time plot (b), light on/off experiment (c), recyclability experiment (d) of SE to SC conversion, and substrate scope analysis with Zn@MA-POP(e). Reaction conditions: catalyst (30 mg), cocatalyst TBAB (0.160 g), epoxide (0.5 mL), 1 bar of CO_2, 250 W xenon lamp, reaction time 8 h.

undergo a fixation process with epoxide to yield cyclic carbonates.

Visible-Light-Assisted CO_2 Photofixation with Zn@MA-POP. To evaluate the photocatalytic activity of Zn@MA-POP, we have performed visible-light-promoted CO_2 photocycloaddition of styrene epoxide (SE) in the presence of tetrabutylammonium bromide (TBAB) as cocatalyst (Figure 5a). The initial reaction begins with by placing 0.5 mL of SE in a 5 mL two-neck round-bottom flask charged with 30 mg of as-synthesized Zn@MA-POP and 0.160 g of TBAB. The final reaction mixture was purged with N_2 followed by CO_2 for 45 min to remove the dissolved air and then inserted into a photoreactor using a 250 W xenon lamp for 8 h with stirring. After the end of the reaction, the obtained reaction mixture was then subjected to GC-MS to get the final percentage of product formation. After the initial 1 h of the reaction (Figure 5b), we observed the formation of the single product styrene carbonate (SC) in a 31% yield. Upon increasing the reaction time, the conversion and SC yield gradually were elevated without any byproduct formation. the SC yield increased from 45% to 61% as the reaction progressed from 2 to 4 h. After 8 h of the reaction, Zn@MA-POP afforded a 91% SC yield under the visible-light irradiation.

Control experiments have been conducted to understand the influence of various parameters in the CO_2 photofixation reaction. At first, we have performed the reaction in the dark at 1 atm of CO_2 pressure for 8 h (entry 2, Table S2 in the Supporting Information). Only 16% SC was obtained after the reaction, clearly illustrating the significance of light illumination for this particular reaction. The activation of CO_2 does not occur adequately in the dark, which is critical for the reaction to proceed. Hence, we got a comparatively less amount of product without the use of light. A very negligible amount of SC formation (8%) was experienced when the reaction was carried out without the cocatalyst TBAB (entry 3, Table S2 in the Supporting Information). In addition, when the reaction was performed only with TBAB in absence of the Zn@MA-POP catalyst (entry 4, Table S2 in the Supporting Information), a poor yield was obtained under identical reaction conditions. Thus, the cocatalyst and catalyst both played pivotal roles in the catalytic transformation process, and the absence of either of them led to a lower yield during the reaction. We have also performed the reaction using the Zn complex (Zn@COM) instead of Zn@MA-POP catalyst (entry 5, Table S2 in the Supporting Information), but the poor yield (20%) demonstrated the significance of the conjugated polymeric framework in Zn@MA-POP for the photocatalytic electron transformation process, which was absent in the parent Zn complex. Further, the reaction under similar conditions without any CO_2 demonstrated a trace amount of product formation (entry 6, Table S2 in the Supporting Information). We have also conducted similar reactions under N_2 and aerobic atmospheres (entries 7 and 8, Table S2 in the Supporting Information), which exhibited a trace amount of epoxide conversion to cyclic carbonate. The local heat produced on the catalyst surface during visible-light illumination was measured and found to be less than 40 °C. We conducted a similar reaction maintaining all the conditions at 40 °C in the absence of light and we obtained only a trace amount of products (entry 9, Table S2 in the Supporting Information). Furthermore, to check the catalytic activity under thermal conditions, we also conducted another reaction at a much higher temperature (60 °C) for 8 h (entry 10, Table S2 in the Supporting Information) in the absence of light. At the end of reaction, there was only 26% epoxide conversion to cyclic carbonate. The overall yield of cyclic carbonate under thermal conditions was much lower than that of photocatalytic conditions under the optimized reaction parameters. This definitely proves the superior performance of our Zn@MA-POP catalyst under light illumination. Moreover, Pescarmona et. al also reported the requirement of higher temperature (100−120 °C) and higher CO_2 pressure to activate CO_2 and epoxide moieties for the reaction to proceed under thermal conditions.[52] This indicated the minimal effect of temperature on our reaction, and the overall CO_2 fixation by Zn@MA-POP catalyst solely depends on the light irradiation. We have performed a similar reaction under visible light irradiation (entry 11, Table S2 in the Supporting Information) using a visible band-pass filter. Under visible-light irradiation the Zn@MA-POP catalyst showed only 40% styrene epoxide conversion to cyclic carbonate, which is comparatively much lower than that of full-spectrum light. A light on/off experiment was performed under the optimum reaction conditions (Figure 5c). At first, the reaction was continued for 1 h under a dark condition, which showed a negligible catalytic conversion of ∼2−3%. After that the reaction was performed under light irradiation for 1 h, resulting in a suitable amount of cyclic carbonate formation. In a similar way, the reaction has been carried out up to 8 h following the light irradiation in every alternate hour. At the end of 8 h, the catalyst showed 91% SE conversion along with 100% SC selectivity. This experiment further established the crucial role of the light in our reaction. The heterogeneous nature of the Zn@MA-POP photocatalyst was confirmed by a recyclability experiment under the optimized reaction conditions (Figure 5d). After the completion of the reaction the photocatalyst was recovered, washed with methanol, dried in an oven at 70 °C, and utilized for the next catalytic run using fresh reactant and cocatalyst for 8 h. The photocatalyst illustrated significant stability up to the sixth catalytic run. An almost indistinguishable reactant and product distribution during recycling experiments clearly demonstrated the excellent stability and robustness of our Zn@MA-POP photocatalyst. To check the structural integrity of reused Zn@MA-POP(R), we have performed wide-angle PXRD, N_2-adsorption/desorption, SEM, and TEM analyses of the photocatalyst after the sixth catalytic cycle (Figure S16 in the Supporting Information). The wide-angle PXRD data (Figure S16a in the Supporting Information) revealed that the amorphous nature of the reused catalyst remains unaltered along with the absence of a ZnO crystalline phase. Notably, after the fifth catalytic cycle, the overall activity decreases to some extent. The main reason behind the diminishment in the catalytic activity was carbon deposition on the catalyst surface, which eventually blocks the catalyst's active sites. Moreover, deposition of reactants and products on the pores of the polymer during catalytic cycles also led to clogging of the pores and eventually decreased the catalyst's activity. Furthermore, the blocking of porous channels *via* carbonaceous deposition was confirmed by a BET surface area analysis (Figure S16b in the Supporting Information). In comparison with the fresh catalyst (158 m^2/g surface area), the reused catalyst showed a lower surface area of 121 m^2/g, indicating that the carbonaceous deposition thereby reduced the accessibility of active sites throughout the porous channel.[53] Furthermore, during the reaction, the contact of the stirrer with the quartz reactor wall may shatter the exposed surface of Zn, which might be another reason for the lowering of product selectivity.[54] We have also conducted an ICP-OES analysis of the Zn@MA-POP after the sixth cycle, which showed 8.38 wt % of Zn, which is relatively lower than that of the fresh catalyst (10.49 wt % Zn), also contributing to the lowering of catalytic activity. Furthermore, the SEM and TEM images (Figure S16c,d in the Supporting Information) showed a similar cluster morphology along with the porous nature of the Zn@MA-POP(R) in comparison to the fresh Zn@MA-POP. This carbon deposition on the rough surface of the fresh catalyst may be one possible reason for the creation of a smooth surface after few cycles, as was experimentally evidenced from the TEM images. Due to Zn@MA-POP's outstanding performance in CO_2 activation and SE conversion, many additional epoxides with different substituents were investigated under the same reaction parameters (Figure 5e and Table S3 in the Supporting Information). Zn@MA-POP exhibited effective CO_2 photofixation to epoxides for the formation of cyclic carbonates irrespective of the substituents. Zn@MA-POP may thus be employed in the majority of CO_2 cycloaddition reactions involving epoxides. To further check the superiority of our as-synthesized Zn@MA-POP catalyst, we have compared the CO_2 insertion reaction with those of

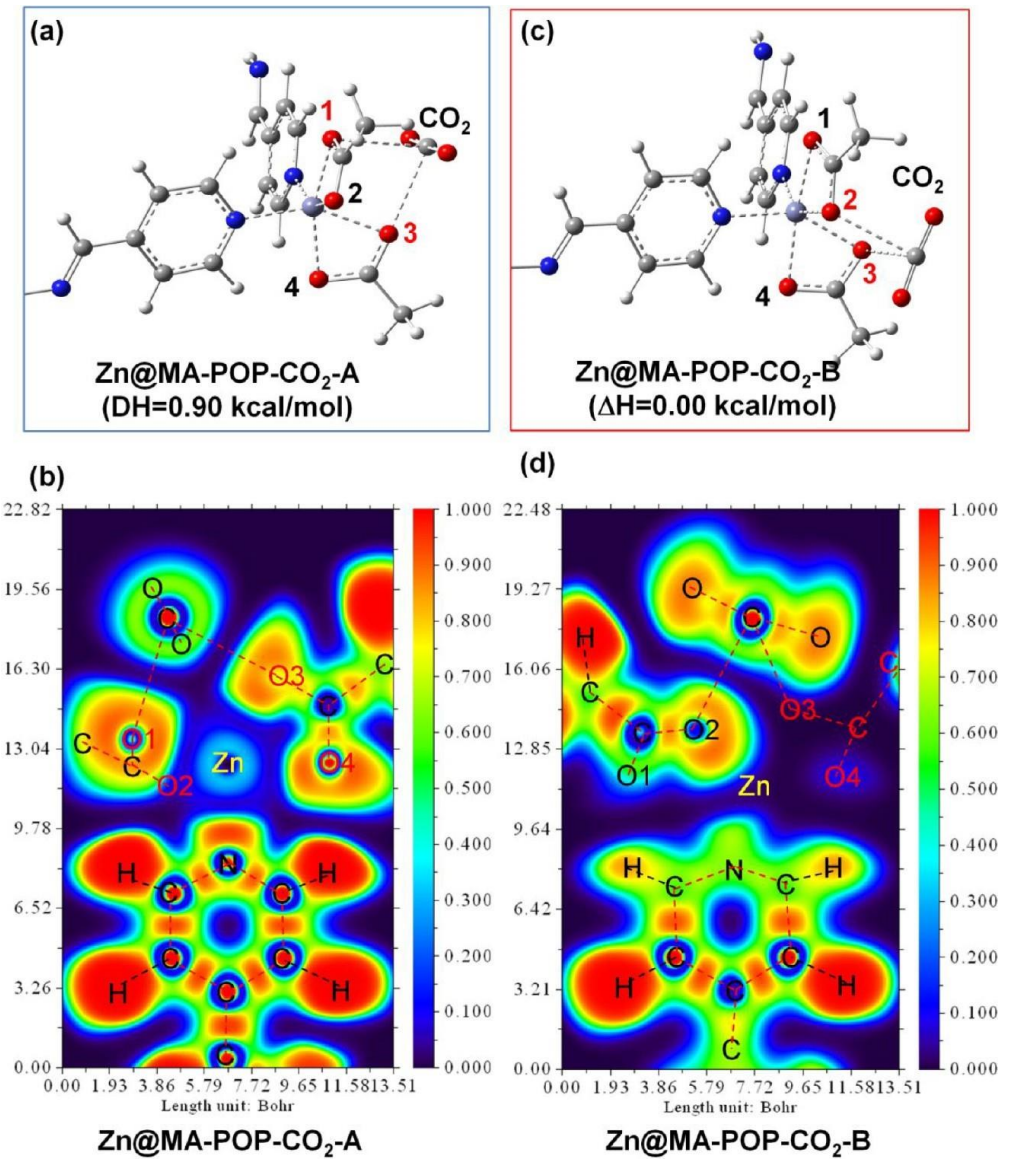

Figure 6. Optimized structures for two interaction complexes of Zn@MA-POP with CO_2 at the O1/O3 position (a), and at the O2/O3 position (c) and the corresponding electron localization function (ELF) density maps (b, d). All calculations were performed at the M06-2X(GD3)/LanL2DZ level of theory.

other Zn-based catalysts such as Zn@COM, Zn@TiO_2, and Zn@g-C_3N_4 (Figure S17 in the Supporting Information). The other catalysts showed comparatively lower conversions of 33%, 26%, and 29% of epoxide to cyclic carbonate, respectively, with respect to Zn@MA-POP. This clearly confirms the superior-light harvesting capacity and higher photoactivity of metalated POPs in comparison to other conventional photocatalysts. Notably, the lower activity of Zn@COM in comparison with the Zn@MA-POP catalyst was later investigated through a density of states (DOS) analysis, which helped to explain the effect of polymerization. We have also compared the photoactivity of Zn@MA-POP with those of previously reported catalysts (Table S4 in the Supporting Information). Huang and co-workers recently developed a unique strategy by incorporating Lewis acidic sites in a metal–organic framework (PCN-224) in order to facilitate ring opening of propylene oxide during a visible-light-promoted CO_2 cycloaddition reaction.[55] Grafting of cobalt phthalocyanine over the semiconductor-based photocatalyst TiO_2 led to the formation of a highly efficient hybrid catalytic system for atmospheric CO_2 insertion into the epoxide ring under solar light illumination.[24] The highly conjugated TaPa-COF system efficiently derived from 2,4,6-triformylphloroglucinol and *p*-phenylenediamine appeared to be a very effective photocatalyst for CO_2 photofixation into cyclic carbonates.[23] One of the most important discoveries in this field was the development of a Zr-thiamine-based carbon nitride (Zr-Thia/g-CN) with optimum Lewis acidic/basic sites to generate a cyclic carbonate on a large scale by incorporating atmospheric CO_2 into the epoxide ring under thermal conditions as well as simulated light irradiation.[22] However, the as-synthesized Zn@MA-POP photocatalyst exhibited a better performance with respect to the reaction time and reaction conditions in comparison with other reported catalytic systems.

Density Functional Theory Calculations. In order to better understand the CO_2 fixation by Zn@MA-POP and the

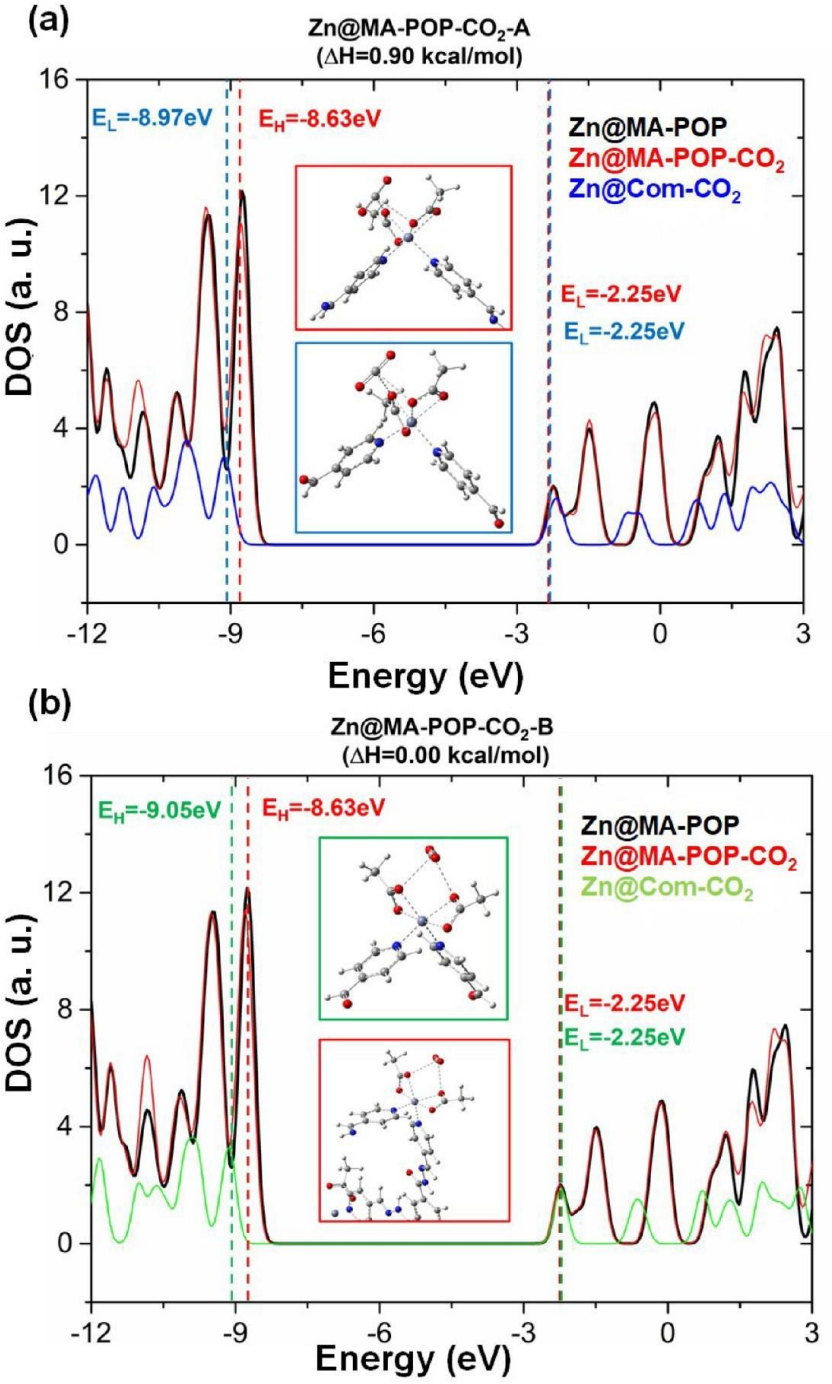

Figure 7. Density of states (DOS) for the complexes of CO_2 with Zn@COM and Zn@MA-POP interacting by two configurations (a) and (b), respectively.

conversion mechanism of SE to SC *via* CO_2 insertion, a DFT analysis was performed. All of the Cartesian coordinates and thermochemical properties of TPH, Zn@COM monomers, Zn@MA-POP polymers and their complexes with CO_2 (Zn@COM-CO_2, Zn@MA-POP) are presented in Table S5 in the Supporting Information. In general, the CO_2 activation by Zn@MA-POP is initiated by complexation of a CO_2 molecule into two different positions O1/O3 (Zn@MA-POP-CO_2-A; Figure 6a and Table S5 in the Supporting Information) or O2/O3 (Zn@MA-POP-CO_2-B; Figure 6c and Table S5 in the Supporting Information) of two methyl carboxylate ligands, of which the latter has a relative energy 0.90 kcal/mol lower than that of the former. Their corresponding electron localization function (ELF) density maps (Figure 6b,d) also show that the interaction of a CO_2 molecule at the O2/O3 position is more polarized than that at the O1/O3 position. Thus, the CO_2 prefers more to interact with Zn@MA-POP polymer at the O2/O3 position.

The densities of states (DOSs) for the complexes of CO_2 with Zn@MA-POP and Zn@COM compared in Figure 7a,b show that the polymer form exhibits a narrower band gap of energy in comparison to the monomer for both interaction

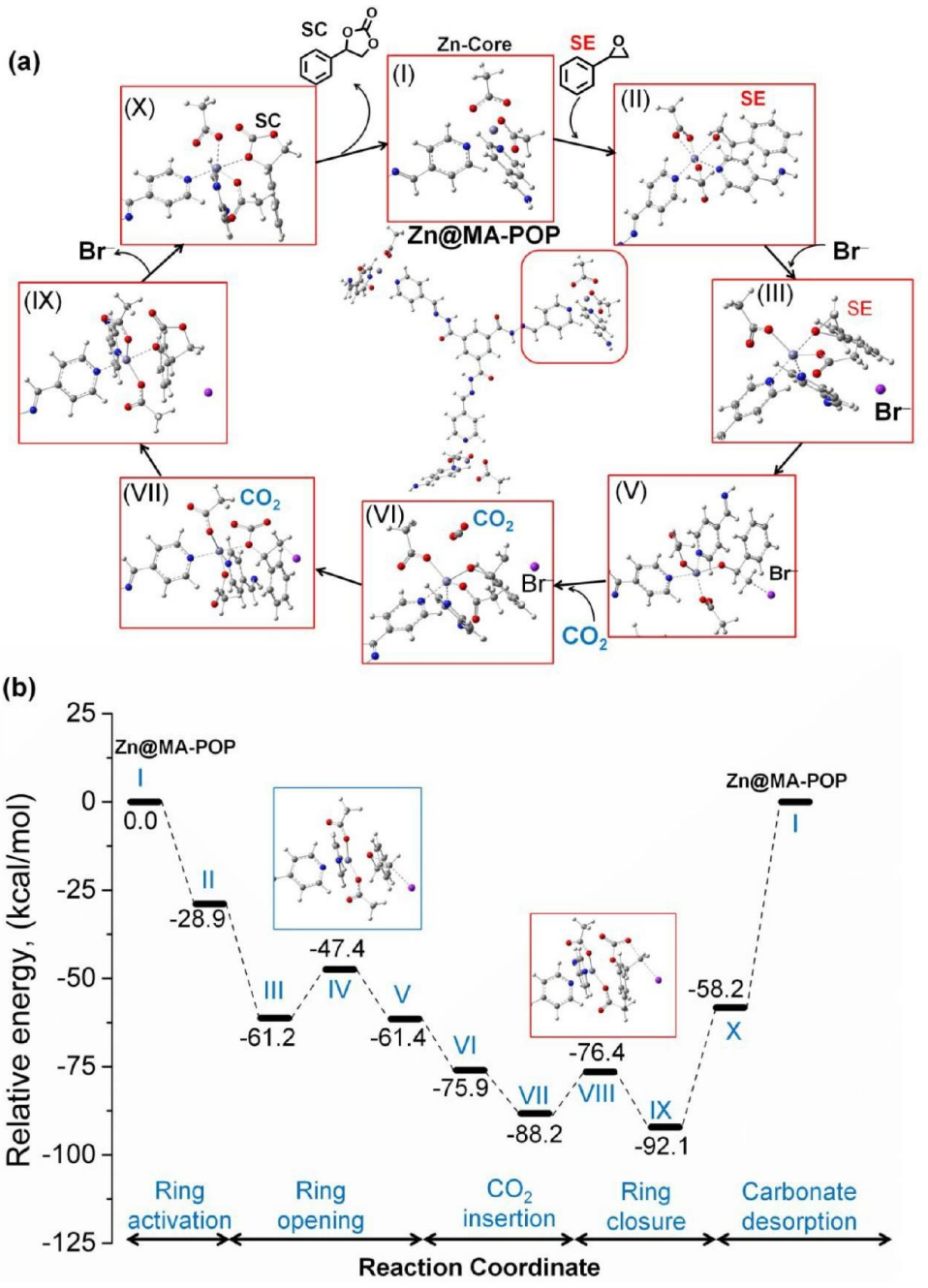

Figure 8. Reaction mechanism for the conversion of SE into SC *via* CO_2 insertion on Zn@MA-POP (a). Potential energy profiles at 298 K for the reaction path calculated at the DFT/M06-2X(GD3)/LanL2DZ level (b).

configurations A and B. For example, in the most stable configuration, i.e., Zn@MA-POP-CO_2-B, the LUMO energy (E_L) for the Zn@MA-POP-CO_2 of −8.36 eV (band gap of 6.11 eV) is higher than that for Zn@COM-CO_2 of −9.05 eV (band gap of 6.80 eV), whereas the HOMO energies (E_H) for both complexes are equal to −2.25 eV (Figure 7). Thus, the polymerization of Zn@MA-POP evidently tends to be responsible for the higher activity of CO_2 activation in comparison to the Zn@COM monomer as observed in the experiments.

Furthermore, the reaction mechanism for the conversion of SE into SC *via* CO_2 insertion on Zn@MA-POP and the DFT/M06-2X(GD3)-calculated potential energy profile is presented in Figure 8a,b. The corresponding Cartesian coordinates and thermochemical properties for all the intermediates and the products are given in Table S6 in the Supporting Information. As can be seen in Figure 8a,b, the most important step of ring activation of SE is initiated by coordination between SE at the O atom with the Zn ion of the Zn@MA-POP to form intermediate II with a relative enthalpy at 298 K that is 28.9 kcal/mol lower than those of the separate initial reactants. Then, the adsorption of the bromide anion (Br^-) generated from TBAB into the less hindered $-CH_2-$ position of the epoxide ring on SE activates the ring-opening reaction of SE, forming intermediate III (relative enthalpy of −61.2 kcal/mol). The ring-opening reaction, which is the rate-determining step, passes the transition state IV (relative energy, −47.4 kcal/mol) with an energy barrier of 13.8 kcal/mol, which is quite

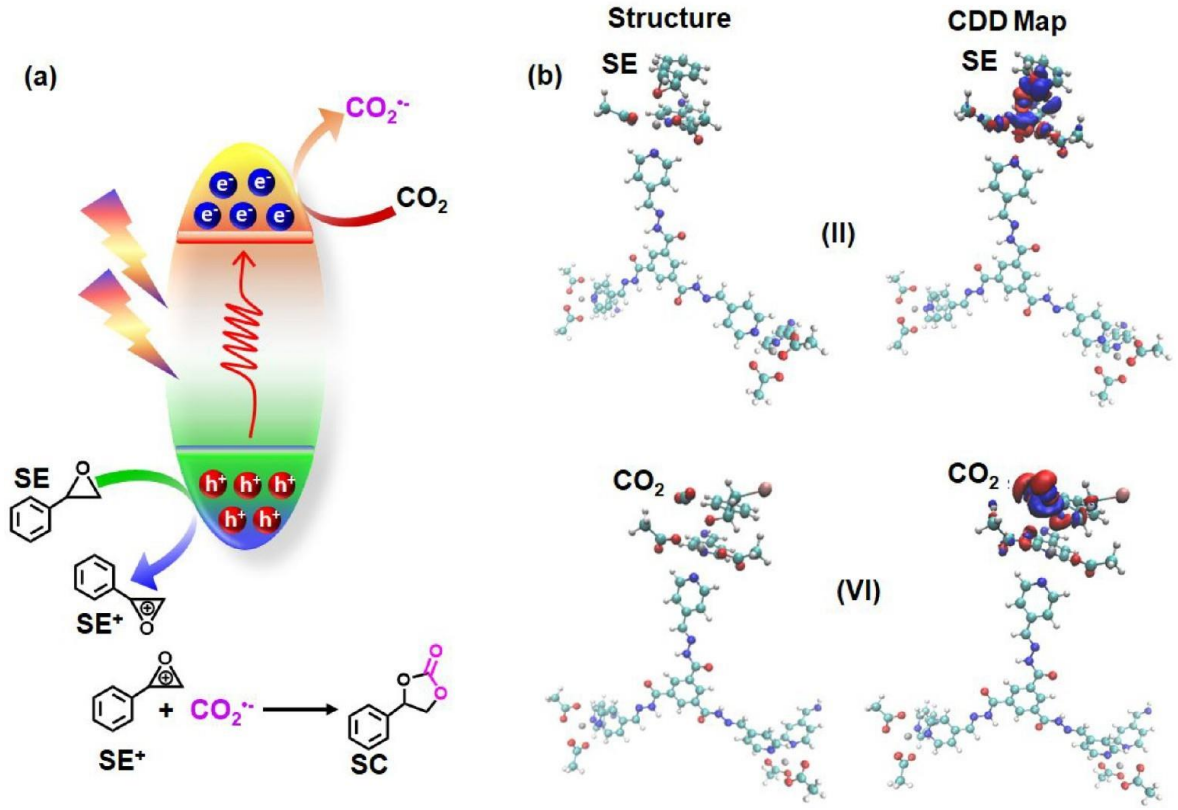

Figure 9. (a) Proposed mechanism for CO_2 cycloaddition by maintaining electron balance. (b) Optimized structures and charge density difference (CDD) maps for complexes II and VI. The red and blue isosurfaces corresponding to +0.001 and −0.001 au respectively represent the regions where the electron density increases and decreases.

lower than that of CO_2 cycloaddition with propylene epoxide catalyzed by 2,5-di-*tert*-butyl-1,4-benzoquinone/5 nm thick conjugated microporous polymer (CMP) nanosheets[56] (i.e., 19.3 kcal/mol). The formed product V possesses an energy equal to −61.4 kcal/mol. The oxygen of the SE moiety with a negative charge becomes a favorable position for the CO_2 insertion step, which is initiated by the formation of a stable complex between the CO_2 molecule and SE (VI) with a relative energy of −75.9 kcal/mol. The CO_2 insertion process does not pass any transition state, and this tends to give the direct formation of intermediate VII (relative enthalpy of −88.2 kcal/mol). The O atom of CO_2 then recombines with the C atom in the methylene $-CH_2-$ group of SE by passing the transition state VIII (−76.4 kcal/mol) with an energy barrier of 11.8 kcal/mol. The product of the ring-closure reaction is the styrene carbonate (SC) in complexation with the Zn@MA-POP and Br^- anion (IX, −92.1 kcal/mol). Finally, the intramolecular displacement of Br^- allows the formation of the cyclic carbonate complex (X, −58.2 kcal/ mol) followed by the SC desorption from the catalyst surface to release the final product SC. It is noteworthy that all of the reactions using our Zn@MA-POP are all spontaneous and exergonic under the studied conditions, and the Zn@MA-POP polymer illustrates a better light-harvesting ability in CO_2 fixation in comparison to its monomeric counterpart (Zn@COM). The relative energies of all the intermediates in the potential energy profiles were also evaluated as function of temperature from 298 to 400 K by using Thermo code[58] in order to shed light on the influence of temperature under light irradiation or the photothermal effect (Table S7 in the Supporting Information). As a result, a negligible increase in relative energy from 0.3 to 0.7 kcal/mol is observed as a function of temperature. The thermodynamic properties of all the species at higher temperature up to 1000K can be found in Table S6 in the Supporting Information.

Wang et al. very recently reported that under photocatalytic conditions the epoxide ring of styrene epoxide (SE) gets oxidized to SE^+ by the photogenerated holes of the valence band (VB) of a Bi oxide/Ti oxide molecular hybrid based photocatalyst with the postulation of an S-scheme.[57] Based on this previous literature report, we also can speculate a relevant concept that the CO_2 molecule gets reduced to $CO_2^{\bullet-}$ by accepting photoexcited electrons from the conduction band (CB) when the Zn@MA-POP catalyst is exposed to the light. In this way eventually both SE and CO_2 get activated under light irradiation and proceed for a further cycloaddition reaction to yield cyclic SC. Figure 9a depicts the photophysical and chemical process for the activation of SE and CO_2. It is worth mentioning that CO_2 cycloaddition involves the initial reduction of CO_2 to $CO_2^{\bullet-}$, followed by fixation in the activated epoxide ring ($SE^{\ddagger}$), but not the conventional CO_2 reduction to other products. Initially, the Zn@MA-POP gets excited by light irradiation and creates photoexcited electrons and holes at the CB and VB, respectively. A time-correlated single photon counting (TCSPC) experiment noted above described a higher lifetime (τ_{avg}) of about 0.86 ns for the photogenerated electrons, indicating the formation of stable excitons (electron−hole pairs) with a lower recombination rate (Figure 4c). Now, the $CO_2^{\bullet-}$ intermediate is formed by transferring an electron from CB to CO_2 followed by the

quenching of holes at the VB by SE to produce SE^+. As a result, the overall electron balance is maintained during the catalytic cycle, which was also considered in our proposed mechanistic pathway as supported by the DFT/M06-2X-(GD3)-calculated potential energy profile (Figure 8). Furthermore, the optimized structures and charge density difference (CDD) maps for SE-Zn@MA-POP (II) and CO_2-SE-Zn@MA-POP (VI) complexes also demonstrate the charge separation in SE and CO_2 during the photocatalytic cycloaddition reaction. As presented in Figure 9b, in complex II, we can notice that the electron densities at SE are decreased (blue isosurfaces) and increase subsequently at other moieties of the respective Zn@MA-POP complex. In contrast, we can also observe that in complex VI the electron densities are reduced at the SE and transferred to the CO_2 molecule, thereby increasing the electron densities at CO_2 (red isosurfaces). This observation from the DFT computational charge density difference (CDD) maps study clearly establishes our hypothesis of an electron transfer mechanism from SE to CO_2 by maintaining the total electron balance.

CONCLUSION

In summary, we have developed a visible-light-responsive Zn-metalated porous organic polymer (Zn@MA-POP) by a monomer-assembly-directed one-pot polycondensation between TPH and Zn@COM monomers. The excellent light-harvesting property, tunable band gap of the conjugated organic framework, and the Zn core (ZnN_2O_4) active site in the as-synthesized Zn@MA-POP are utilized for the solar-light-driven CO_2 photofixation. The obtained Zn@MA-POP exhibited higher photocatalytic activity toward insertion of CO_2 into oxiranes in comparison to the parent Zn@COM as a consequence of extended π conjugation in the porous organic polymer, which not only accommodates the Zn active site to prevent further agglomeration but also maximizes the light absorption capacity to overcome all the disadvantages related to commercially available conventional semiconductor photocatalysts. A DFT study unveiled the crucial information about CO_2 activation by Zn@MA-POP through two different complexation strategies (Zn@MA-POP-CO_2-A and Zn@ MA-POP-CO_2-B), where the former exhibited a higher relative energy (0.90 kcal/mol) in comparison to the latter. Moreover, the formation of SC from SE over Zn@MA-POP involving several intermediates in the mechanistic pathway was spontaneous and exergonic in nature. On the other hand, the density of states (DOS) for the complexes of CO_2 with Zn@MA-POP and Zn@COM exhibited a narrower band gap energy in comparison to the monomer counterpart, whereas the LUMO energies (E_L) for Zn@MA-POP-CO_2 and Zn@COM-CO_2 were −8.36 and −9.05 eV with the corresponding band gaps 6.11 and 6.80 eV, respectively, clearly demonstrating the involvement of the polymeric network in the electron transfer process. Thus, the novel photocatalyst Zn@MA-POP for the chemical fixation of CO_2 into a cyclic epoxide has been developed and the structure−activity relationship was also established with the help of an EXAFS and DFT study, utterly important in this modern era for CO_2 mitigation to prevent environmental pollution.

EXPERIMENTAL SECTION

Synthesis of Zn@MA-POP Photocatalyst. In order to synthesize a molecular-assembly-based metalated porous organic polymer, 1.5 mmol of a zinc pyridine complex (Zn@COM, 0.596 g) and 1 mmol of TPH were dissolved in 20 mL of DMAc and then 2.5 mL of 6 M acetic acid was added to initiate the Schiff base reaction. After that, the resulting solution was subjected to continuous heating and stirring for 72 h at 130 °C under an N_2 atmosphere. After completion of the reaction, the resulting yellow solution was cooled to room temperature and a yellow precipitate was obtained in methanol. Finally, the precipitate was washed with methanol and dried in an oven, denoted Zn@MA-POP. The overall synthetic procedure is depicted in Figure S3 in the Supporting Information.

Synchrotron-Radiation-Based XAS Measurements and Data Analysis. The Zn K-edge X-ray absorption fine structure (XAFS) measurements were performed at the B18 beamline at the Diamond Light Source, UK. Pellets for the measurements were made by homogeneously mixing the sample with an inert cellulose matrix to have an X-ray absorption edge jump of close to 1. A standard data analysis procedure was used to extract the extended X-ray absorption fine structure (EXAFS) signal from the measured absorption spectra. Background subtraction, normalization, and alignment of the XAFS data were performed with ATHENA software.

General Procedure for Photocatalytic Conversion of Epoxides to Cyclic Carbonate. Styrene epoxide (0.5 mL, 4 mmol), Zn@MA-POP (30 mg), and TBAB (160 mg, 0.5 mmol) were charged into a 10 mL glass reactor with a stir bar. After that, N_2 gas was purged to the reaction mixture in order to remove the air followed by the addition of a balloon containing high-purity CO_2. Finally, the reaction mixture was irradiated with a 250 W Xe lamp for several hours at room temperature. The catalyst was isolated by filtration after the completion of the reaction and the solution of the product was extracted from the filtrate by ethyl acetate and water (1:1). Further, the as-collected solution was analyzed by GC-MS to detect the unreacted epoxides and cyclic carbonate products. Notably, all the reactions were carried out in an air-conditioned room (22 °C) and an infrared temperature gun (GM320) was used to measure the local heat produced on the catalyst surface during visible-light illumination. It was found that the heat produced on the catalyst surface during light irradiation was less than 40 °C. For the visible-light spectrum we used a visible band-pass filter (Newport, FSQ-KG1) attached to the 250 W Xe lamp.

DFT Calculations. The density functional theory (DFT) analysis was performed with the D3 version of Grimme's dispersion with the original D3 damping function (GD3) using the M06-2X functional combined with the LanL2DZ basis set and was employed using Gaussian 16 Rev. C.01. The CDD map was calculated by the MultiWfn code. All images were visualized by VMD software. C, N, O, Zn, and H atoms correspond to turquoise, blue, red, gray, and light gray balls.

ASSOCIATED CONTENT

Supporting Information

The Supporting Information is available free of charge at https://pubs.acs.org/doi/10.1021/acsami.2c06982.

Materials and methods for other synthesis procedures, product analysis by gas chromatography (GC/GC-MS), catalyst recyclability test, characterization techniques, wide-angle powder X-ray diffraction pattern (PXRD), FT-IR analysis, estimation of the isosteric heats of CO_2 gas adsorption, the CO_2 adsorption isotherms with the virial equation fits (lines) and isosteric heat of adsorption, thermogravimetric analysis (TGA), FE-SEM images of the TPH monomer, energy dispersive X-ray (EDX) spectroscopy, X-ray photoelectron spectroscopy (XPS) survey spectrum, deconvoluted C 1s, N 1s, and O 1s XPS spectra, parameters of the TRPL decay, Tauc plots, optimized structure (HOMO−LUMO) and corresponding ESP map, controlled CO_2 photofixation, PXRD, N_2 adsorption−desorption isotherm, FE-SEM and TEM images of reused photo-

catalyst, substrate scopes, comparison study with various Zn-based catalysts, previous reports of photocatalytic CO_2 fixation, Cartesian coordinates and thermochemical properties for TPH, Zn@COM monomers, and Zn@MA-POP polymer, Cartesian coordinates, thermochemical properties for the intermediates of the reaction pathway for the conversion of styrene epoxide (SE) into styrene carbonate (SC) *via* CO_2 insertion on Zn@MA-POP, energy (HF), zero-point vibrational energy (ZPE), thermal correction to enthalpy (ddH), entropy (S^0) and relative enthalpies at 0, 298, 300, 350, and 400 K for different intermediates in the reaction pathway of the conversion of styrene epoxide (SE) to styrene carbonate (SC) *via* Zn@MA-POP material, and ^1H and ^{13}C NMR spectra of Zn@COM monomer (PDF)

AUTHOR INFORMATION

Corresponding Author

John Mondal − *Department of Catalysis & Fine Chemicals, CSIR-Indian Institute of Chemical Technology, Hyderabad 500007, India; Academy of Scientific and Innovative Research (AcSIR), Ghaziabad 201002, India;* orcid.org/0000-0001-7813-2108; Email: johncuchem@gmail.com, johnmondal@iict.res.in

Authors

Chitra Sarkar − *Department of Catalysis & Fine Chemicals, CSIR-Indian Institute of Chemical Technology, Hyderabad 500007, India; Academy of Scientific and Innovative Research (AcSIR), Ghaziabad 201002, India;* orcid.org/0000-0003-0472-7728

Ratul Paul − *Department of Catalysis & Fine Chemicals, CSIR-Indian Institute of Chemical Technology, Hyderabad 500007, India; Academy of Scientific and Innovative Research (AcSIR), Ghaziabad 201002, India;* orcid.org/0000-0002-9920-9204

Duy Quang Dao − *Institute of Research and Development and Faculty of Natural Sciences, Duy Tan University, Da Nang 550000, Vietnam;* orcid.org/0000-0003-0896-5168

Shaojun Xu − *Cardiff Catalysis Institute, School of Chemistry, Cardiff University, Cardiff CF10 3AT, U.K.; UK Catalysis Hub, Research Complex at Harwell, Rutherford Appleton Laboratory, Harwell OX11 0FA, U.K.;* orcid.org/0000-0002-8026-8714

Rupak Chatterjee − *School of Materials Science, Indian Association for the Cultivation of Science, Kolkata 700032, India;* orcid.org/0000-0002-3325-7895

Subhash Chandra Shit − *Department of Catalysis & Fine Chemicals, CSIR-Indian Institute of Chemical Technology, Hyderabad 500007, India; Academy of Scientific and Innovative Research (AcSIR), Ghaziabad 201002, India;* orcid.org/0000-0002-9971-3179

Asim Bhaumik − *School of Materials Science, Indian Association for the Cultivation of Science, Kolkata 700032, India;* orcid.org/0000-0002-4907-7418

Author Contributions

° C.S. and R.P. have equally contributed to this work.

Notes

The authors declare no competing financial interest.

ACKNOWLEDGMENTS

C.S. and R.P. acknowledge the University Grants Commission (UGC) and DST-INSPIRE (GAP-0799), for their respective senior research fellowships (SRF) at CSIR-IICT, Hyderabad. J.M. acknowledges the Council of Scientific & Industrial Research (CSIR) India, for the CSIR-Young Research Award (YSA) Grant (reference no. HRDG/YSA-19/02/21(0045)/2019) and CSIR-Focused Basic Research (FBR) Grant under the CLP theme (reference no. 34/1/TD-CLP/NCP-FBR 2020-RPPBDD-TMD-SeMI) for financial support at CSIR-IICT, Hyderabad. D.Q.D. acknowledges SEAGrid (http:www.seagrid.org) for the computational resources and services for the selected results used in this publication. S.X. is thankful for resources and support provided via our membership in the UK Catalysis Hub Consortium and funded by EPSRC grants: EP/R026939/1, EP/R026815/1, EP/R026645/1, EP/R027129/1, and EP/M013219/1(biocatalysis). We sincerely thank Dr. Rajaram Bal, Council of Scientific and Industrial Research-Indian Institute of Petroleum (CSIR-IIP), Dehradun for NH_3-TPD experiments. We are also very much grateful to the Director, CSIR-IICT (no. IICT/Pubs./2022/133), for support.

REFERENCES

(1) Navarro-Jaén, S.; Virginie, M.; Bonin, J.; Robert, M.; Wojcieszak, R.; Khodakov, A. Y. Highlights and Challenges in the Selective Reduction of Carbon Dioxide to Methanol. *Nat. Rev. Chem.* **2021**, *5* (8), 564−579.

(2) Qu, Y.; Duan, X. One-dimensional Homogeneous and Heterogeneous Nanowires for Solar Energy Conversion. *J. Mater.-Chem.* **2012**, *22* (32), 16171−16181.

(3) Hurst, T. F.; Cockerill, T. T.; Florin, N. H. Life Cycle Greenhouse Gas Assessment of a Coal-fired Power Station with Calcium Looping CO_2 Capture and Offshore Geological Storage. *Energy Environ. Sci.* **2012**, *5* (5), 7132−7150.

(4) Das, N.; Paul, R.; Dao, D. Q.; Chatterjee, R.; Borah, K.; Chandra Shit, S.; Bhaumik, A.; Mondal, J. Nanospace Engineering of Triazine-Thiophene-Intertwined Porous-Organic-Polymers via Molecular Expansion in Tweaking CO_2 Capture. *ACS Appl. Nano Mater.* **2022**, *5* (4), 5302−5315.

(5) Kim, Y. H.; Kim, N.; Seo, J.-M.; Jeon, J.-P.; Noh, H.-J.; Kweon, D. H.; Ryu, J.; Baek, J.-B. Benzothiazole-Based Covalent Organic Frameworks with Different Symmetrical Combinations for Photocatalytic CO_2 Conversion. *Chem. Mater.* **2021**, *33* (22), 8705−8711.

(6) Aresta, M.; Dibenedetto, A.; Angelini, A. Catalysis for the Valorization of Exhaust Carbon: from CO_2 to Chemicals, Materials, and Fuels. Technological use of CO_2. *Chem. Rev.* **2014**, *114* (3), 1709−1742.

(7) Fukuoka, S.; Fukawa, I.; Tojo, M.; Oonishi, K.; Hachiya, H.; Aminaka, M.; Hasegawa, K.; Komiya, K. A Novel Non-Phosgene Process for Polycarbonate Production from CO_2: Green and Sustainable Chemistry in Practice. *Catal. Surv. Asia* **2010**, *14* (3), 146−163.

(8) Nohra, B.; Candy, L.; Blanco, J.-F.; Guerin, C.; Raoul, Y.; Mouloungui, Z. From Petrochemical Polyurethanes to Biobased Polyhydroxyurethanes. *Macromolecules* **2013**, *46* (10), 3771−3792.

(9) Liu, D.; Li, G.; Liu, J.; Wei, Y.; Guo, H. Mesoporous Titanium-Silicalite Zeolite Containing Organic Templates as a Bifunctional Catalyst for Cycloaddition of CO_2 and Epoxides. *ACS Appl. Mater. Interfaces* **2018**, *10* (26), 22119−22129.

(10) Srivastava, R.; Srinivas, D.; Ratnasamy, P. CO_2 Activation and Synthesis of Cyclic Carbonates and Alkyl/aryl Carbamates over Adenine-modified Ti-SBA-15 Solid Catalysts. *J. Catal.* **2005**, *233* (1), 1−15.

(11) Yamaguchi, K.; Ebitani, K.; Yoshida, T.; Yoshida, H.; Kaneda, K. Mg-Al Mixed Oxides as Highly Active Acid-Base Catalysts for

Cycloaddition of Carbon Dioxide to Epoxides. *J. Am. Chem. Soc.* **1999**, *121* (18), 4526−4527.
(12) Zhu, M.; Srinivas, D.; Bhogeswararao, S.; Ratnasamy, P.; Carreon, M. A. Catalytic Activity of ZIF-8 in the Synthesis of Styrene Carbonate from CO_2 and Styrene Oxide. *Catal. Commun.* **2013**, *32*, 36−40.
(13) Wang, H.-H.; Hou, L.; Li, Y.-Z.; Jiang, C.-Y.; Wang, Y.-Y.; Zhu, Z. Porous MOF with Highly Efficient Selectivity and Chemical Conversion for CO_2. *ACS Appl. Mater. Interfaces* **2017**, *9* (21), 17969−17976.
(14) Li, M.; Ren, H.; Sun, F.; Tian, Y.; Zhu, Y.; Li, J.; Mu, X.; Xu, J.; Deng, F.; Zhu, G. Construction of Porous Aromatic Frameworks with Exceptional Porosity via Building Unit Engineering. *Adv. Mater.* **2018**, *30* (43), 1804169.
(15) Carta, M.; Malpass-Evans, R.; Croad, M.; Rogan, Y.; Jansen, J. C.; Bernardo, P.; Bazzarelli, F.; McKeown, N. B. An Efficient Polymer Molecular Sieve for Membrane Gas Separations. *Science* **2013**, *339* (6117), 303−307.
(16) Wang, S.; Xu, M.; Peng, T.; Zhang, C.; Li, T.; Hussain, I.; Wang, J.; Tan, B. Porous hypercrosslinked polymer-TiO_2-graphene composite photocatalysts for visible-light-driven CO_2 conversion. *Nat. Commun.* **2019**, *10* (1), 676.
(17) Zhang, Y.-Y.; Yang, G.-W.; Xie, R.; Yang, L.; Li, B.; Wu, G.-P. Scalable, Durable, and Recyclable Metal-Free Catalysts for Highly Efficient Conversion of CO_2 to Cyclic Carbonates. *Angew. Chem., Int. Ed.* **2020**, *59* (51), 23291−23298.
(18) Paul, R.; Shit, S. C.; Singh, A.; Wong, R. J.; Dao, D. Q.; Joseph, B.; Liu, W.; Bhattacharya, S.; Mondal, J. Organogel-assisted Porous Organic Polymer Embedding Cu NPs for Selectivity Control in the Semi Hydrogenation of Alkynes. *Nanoscale* **2022**, *14* (4), 1505−1519.
(19) Paul, R.; Chandra Shit, S.; Mandal, H.; Rabeah, J.; Kashyap, S. S.; Nailwal, Y.; Shinde, D. B.; Lai, Z.; Mondal, J. Benzothiazole-Linked Metal-Free Covalent Organic Framework Nanostructures for Visible-Light-Driven Photocatalytic Conversion of Phenylboronic Acids to Phenols. *ACS Appl. Nano Mater.* **2021**, *4* (11), 11732−11742.
(20) Zhang, Z.; Jia, J.; Zhi, Y.; Ma, S.; Liu, X. Porous Organic Polymers for Light-driven Organic Transformations. *Chem. Soc. Rev.* **2022**, *51* (7), 2444−2490.
(21) Sarkar, P.; Hazra Chowdhury, A.; Biswas, S.; Khan, A.; Islam, S. M. 2D Covalent Organic Framework: a Photoactive Heterogeneous Catalyst for Chemical Fixation of CO_2 over Propargyl Amines in Water Under Sunlight. *Mater. Today Chem.* **2021**, *21*, 100509.
(22) Kumar, A.; Samanta, S.; Srivastava, R. Graphitic Carbon Nitride Modified with Zr-Thiamine Complex for Efficient Photocatalytic CO_2 Insertion to Epoxide: Comparison with Traditional Thermal Catalysis. *ACS Appl. Nano Mater.* **2021**, *4* (7), 6805−6820.
(23) Das, A.; Mondal, R. K.; Chakrabortty, P.; Riyajuddin, S.; Chowdhury, A. H.; Ghosh, S.; Khan, A.; Ghosh, K.; Islam, S. M. Visible Light Assisted Chemical Fixation of Atmospheric CO_2 into Cyclic Carbonates using Covalent Organic Framework as a Potential Photocatalyst. *Mol. Catal.* **2021**, *499*, 111253.
(24) Prajapati, P. K.; Kumar, A.; Jain, S. L. First Photocatalytic Synthesis of Cyclic Carbonates from CO_2 and Epoxides Using CoPc/TiO_2 Hybrid under Mild Conditions. *ACS Sustain. Chem. Eng.* **2018**, *6* (6), 7799−7809.
(25) Liu, T.-T.; Lin, Z.-J.; Shi, P.-C.; Ma, T.; Huang, Y.-B.; Cao, R. A Metallosalen-based Porous Organic Polymer for Olefin Epoxidation. *ChemCatChem.* **2015**, *7* (15), 2340−2345.
(26) Zhang, W.; Cui, T.; Bi, S.; Ma, L.; Lu, D.; Wu, D.; Zhang, F. A Monomer-Assembly Template-Directed Synthesis of Conjugated Porous Polymer Microtubular Bundles. *Mater. Horiz.* **2020**, *7* (2), 551−558.
(27) Li, H.; Li, C.; Chen, J.; Liu, L.; Yang, Q. Synthesis of a Pyridine-Zinc-Based Porous Organic Polymer for the Co-catalyst-Free Cycloaddition of Epoxides. *Chem.: Asian J.* **2017**, *12* (10), 1095−1103.
(28) Li, C.; Liu, J.; Li, H.; Wu, K.; Wang, J.; Yang, Q. Covalent Organic Frameworks with High Quantum Efficiency in Sacrificial Photocatalytic Hydrogen Evolution. *Nat. Commun.* **2022**, *13* (1), 2357.
(29) Liu, K.; Xu, Z.; Huang, H.; Zhang, Y.; Liu, Y.; Qiu, Z.; Tong, M.; Long, Z.; Chen, G. *In situ* Synthesis of Pyridinium-based Ionic Porous Organic Polymers with Hydroxide Anions and Pyridinyl Radicals for Halogen-free Catalytic Fixation of Atmospheric CO_2. *Green Chem.* **2022**, *24* (1), 136−141.
(30) Weng, J.-Y.; Xu, Y.-L.; Song, W.-C.; Zhang, Y.-H. Tuning the Adsorption and Fluorescence Properties of Aminal-linked Porous Organic Polymers through N-heterocyclic Group Decoration. *J. Polym. Sci.* **2016**, *54* (12), 1724−1730.
(31) Centomo, P.; Zecca, M.; Zoleo, A.; Maniero, A. L.; Canton, P.; Jerábek, K.; Corain, B. Cross-linked Polyvinyl Polymersversus Polyureas as Designed Supports for Catalytically Active M^0 Nanoclusters Part III. Nanometer Scale Structure of the Cross-linked Polyurea Support EnCat 30 and of the Pd^{II}/EnCat 30 and Pd^0/EnCat 30NP Catalysts. *Phys. Chem. Chem. Phys.* **2009**, *11* (20), 4068−4076.
(32) Dai, W.; Tian, N.; Liu, C.; Yu, L.; Liu, Q.; Ma, N.; Zhao, Y. (Zn, Ni, Cu)-BTC Functionalized with Phosphotungstic Acid for Adsorptive Desulfurization in the Presence of Benzene and Ketone. *Energy Fuels* **2017**, *31* (12), 13502−13508.
(33) Adet, N.; Specklin, D.; Gourlaouen, C.; Damiens, T.; Jacques, B.; Wehmschulte, R. J.; Dagorne, S. Towards Naked Zinc(II) in the Condensed Phase: A Highly Lewis Acidic Zn^{II} Dication Stabilized by Weakly Coordinating Carborate Anions. *Angew. Chem., Int. Ed.* **2021**, *60* (4), 2084−2088.
(34) Chen, H.; Liu, W.; Qin, Z. ZnO/$ZnFe_2O_4$ Nanocomposite as a Broad-Spectrum Photo-Fenton-like Photocatalyst with Near-Infrared Activity. *Catal. Sci. Technol.* **2017**, *7* (11), 2236−2244.
(35) Sivaranjini, B.; Mangaiyarkarasi, R.; Ganesh, V.; Umadevi, S. Vertical Alignment of Liquid Crystals Over a Functionalized Flexible Substrate. *Sci. Rep.* **2018**, *8* (1), 8891.
(36) Fujimoto, A.; Yamada, Y.; Koinuma, M.; Sato, S. Origins of sp^3C peaks in C_{1s} X-ray Photoelectron Spectra of Carbon Materials. *Anal. Chem.* **2016**, *88* (12), 6110−6114.
(37) Bhunia, S.; Das, S. K.; Jana, R.; Peter, S. C.; Bhattacharya, S.; Addicoat, M.; Bhaumik, A.; Pradhan, A. Electrochemical Stimuli-Driven Facile Metal-Free Hydrogen Evolution from Pyrene-Porphyrin-Based Crystalline Covalent Organic Framework. *ACS Appl. Mater. Interfaces* **2017**, *9* (28), 23843−23851.
(38) Gao, X.; Li, Y.; Yang, X.; Shang, Y.; Wang, Y.; Gao, B.; Wang, Z. Highly Permeable and Antifouling Reverse Osmosis Membranes with Acidified Graphitic Carbon Nitride Nanosheets as Nanofillers. *J. Mater. Chem.* **2017**, *5* (37), 19875−19883.
(39) Moon, I. K.; Lee, J.; Lee, H. Highly Qualified Reduced Graphene Oxides: the best Chemical Reduction. *Chem. Commun.* **2011**, *47* (34), 9681−9683.
(40) Li, F.; Li, W.; Li, J.; Xue, W.; Wang, Y.; Zhao, X. Investigation of Supported $Zn(OAc)_2$ Catalyst and its Stability in N-phenyl Carbamate Synthesis. *Appl. Catal. A-Gen.* **2014**, *475*, 355−362.
(41) Gong, Y.-N.; Zhong, W.; Li, Y.; Qiu, Y.; Zheng, L.; Jiang, J.; Jiang, H.-L. Regulating Photocatalysis by Spin-State Manipulation of Cobalt in Covalent Organic Frameworks. *J. Am. Chem. Soc.* **2020**, *142* (39), 16723−16731.
(42) Han, X.; Wu, X.; Deng, Y.; Liu, J.; Lu, J.; Zhong, C.; Hu, W. Ultrafine Pt Nanoparticle-Decorated Pyrite-Type CoS_2 Nanosheet Arrays Coated on Carbon Cloth as a Bifunctional Electrode for Overall Water Splitting. *Adv. Energy Mater.* **2018**, *8* (24), 1800935.
(43) Demongeot, A.; Mougnier, S. J.; Okada, S.; Soulié-Ziakovic, C.; Tournilhac, F. Coordination and Ctalysis of Zn^{2+} in Epoxy-based Vitrimers. *Polym. Chem.* **2016**, *7* (27), 4486−4493.
(44) Yang, S.; Hu, W.; Zhang, X.; He, P.; Pattengale, B.; Liu, C.; Cendejas, M.; Hermans, I.; Zhang, X.; Zhang, J.; Huang, J. 2D Covalent Organic Frameworks as Intrinsic Photocatalysts for Visible Light-Driven CO_2 Reduction. *J. Am. Chem. Soc.* **2018**, *140* (44), 14614−14618.
(45) Guo, W.; Ding, H.; Su, B. Electrochemiluminescence of Metallated Porous Organic Polymers. *J. Electroanal. Chem.* **2018**, *818*, 176−180.

(46) Shu, C.; Han, C.; Yang, X.; Zhang, C.; Chen, Y.; Ren, S.; Wang, F.; Huang, F.; Jiang, J.-X. Boosting the Photocatalytic Hydrogen Evolution Activity for D-π-A Conjugated Microporous Polymers by Statistical Copolymerization. *Adv. Mater.* 2021, *33* (26), 2008498.
(47) Zhang, J.; Zhang, M.; Sun, R.-Q.; Wang, X. A Facile Band Alignment of Polymeric Carbon Nitride Semiconductors to Construct Isotype Heterojunctions. *Angew. Chem., Int. Ed.* 2012, *51* (40), 10145−10149.
(48) Fu, J.; Zhu, B.; Jiang, C.; Cheng, B.; You, W.; Yu, J. Hierarchical Porous O-Doped g-C_3N_4 with Enhanced Photocatalytic CO_2 Reduction Activity. *Small* 2017, *13* (15), 1603938.
(49) Samanta, S.; Satpati, B.; Srivastava, R. Unraveling the Impact of the Pd Nanoparticle@$BiVO_4$/S-CN Heterostructure on the Photo-Physical & Opto-Electronic Properties for Enhanced Catalytic Activity in Water Splitting and One-pot Three-step Tandem Reaction. *Nanoscale Adv.* 2019, *1* (4), 1395−1412.
(50) Sheng, J.-L.; Dong, H.; Meng, X.-B.; Tang, H.-L.; Yao, Y.-H.; Liu, D.-Q.; Bai, L.-L.; Zhang, F.-M.; Wei, J.-Z.; Sun, X.-J. Effect of Different Functional Groups on Photocatalytic Hydrogen Evolution in Covalent-Organic Frameworks. *ChemCatChem.* 2019, *11* (9), 2313−2319.
(51) Bakiro, M.; Hussein Ahmed, S.; Alzamly, A. Efficient Visible-Light Photocatalytic Cycloaddition of CO_2 and Propylene Oxide Using Reduced Graphene Oxide Supported $BiNbO_4$. *ACS Sustain. Chem. Eng.* 2020, *8* (32), 12072−12079.
(52) Kamphuis, A. J.; Picchioni, F.; Pescarmona, P. P. CO_2-Fixation into Cyclic and Polymeric Carbonates: Principles and Applications. *Green Chem.* 2019, *21* (3), 406−448.
(53) Paul, R.; Shit, S. C.; Fovanna, T.; Ferri, D.; Srinivasa Rao, B.; Gunasooriya, G. T. K. K.; Dao, D. Q.; Le, Q. V.; Shown, I.; Sherburne, M. P.; Trinh, Q. T.; Mondal, J. Realizing Catalytic Acetophenone Hydrodeoxygenation with Palladium-Equipped Porous Organic Polymers. *ACS Appl. Mater. Interfaces* 2020, *12* (45), 50550−50565.
(54) Shit, S. C.; Koley, P.; Joseph, B.; Marini, C.; Nakka, L.; Tardio, J.; Mondal, J. Porous Organic Polymer-Driven Evolution of High-Performance Cobalt Phosphide Hybrid Nanosheets as Vanillin Hydrodeoxygenation Catalyst. *ACS Appl. Mater. Interfaces* 2019, *11* (27), 24140−24153.
(55) Zhai, G.; Liu, Y.; Lei, L.; Wang, J.; Wang, Z.; Zheng, Z.; Wang, P.; Cheng, H.; Dai, Y.; Huang, B. Light-Promoted CO_2 Conversion from Epoxides to Cyclic Carbonates at Ambient Conditions over a Bi-Based Metal-Organic Framework. *ACS Catal.* 2021, *11* (4), 1988−1994.
(56) Zhang, X.; Liu, H.; An, P.; Shi, Y.; Han, J.; Yang, Z.; Long, C.; Guo, J.; Zhao, S.; Zhao, K.; Yin, H.; Zheng, L.; Zhang, B.; Liu, X.; Zhang, L.; Li, G.; Tang, Z. Delocalized Electron Effect on Single Metal Sites in Ultrathin Conjugated Microporous Polymer Nanosheets for Boosting CO_2 Cycloaddition. *Sci. Adv.* 2020, *6* (17), eaaz4824.
(57) Liu, C.; Niu, H.; Wang, D.; Gao, C.; Said, A.; Liu, Y.; Wang, G.; Tung, C.-H.; Wang, Y. S-Scheme Bi-oxide/Ti-oxide Molecular Hybrid for Photocatalytic Cycloaddition of Carbon Dioxide to Epoxides. *ACS Catal.* 2022, *12*, 8202−8213.
(58) Irikura, K. K. THERMO.PY, National Institute of Standards and Technology, 2020. https://www.nist.gov/mml/csd/chemical-informatics-research-group/products-andservices/program-computing-ideal-gas.